



Title	An Examination of the Sea Ice Rheology for Seasonal Ice Zones Based on Ice Drift and Thickness Observations
Author(s)	Toyota, Takenobu; Kimura, Noriaki
Citation	Journal of Geophysical Research Oceans, 123(2), 1406-1428 https://doi.org/10.1002/2017JC013627
Issue Date	2018-02-05
Doc URL	http://hdl.handle.net/2115/71230
Type	article
File Information	JournalofGeophysicalResearch_Oceans_123(2)1406-1428.pdf



[Instructions for use](#)

RESEARCH ARTICLE

10.1002/2017JC013627

An Examination of the Sea Ice Rheology for Seasonal Ice Zones Based on Ice Drift and Thickness Observations

Takenobu Toyota¹  and Noriaki Kimura²¹Institute of Low Temperature Science, Hokkaido University, Sapporo, Japan, ²Atmosphere and Ocean Research Institute, The University of Tokyo, Kashiwa, Japan

Key Points:

- The validity of Hibler's sea ice rheology was examined for the Sea of Okhotsk, the seasonal ice zone, in comparison with the Beaufort Sea
- The algorithm to estimate ice thickness from L-band SAR backscatter was evaluated for the Sea of Okhotsk
- While Hibler's sea ice rheology seems applicable, a grid size in models should be chosen carefully to parameterize the deformation field

Correspondence to:

T. Toyota,
toyota@lowtem.hokudai.ac.jp

Citation:

Toyota, T., & Kimura, N. (2018). An examination of the sea ice rheology for seasonal ice zones based on ice drift and thickness observations. *Journal of Geophysical Research: Oceans*, 123, 1406–1428. <https://doi.org/10.1002/2017JC013627>

Received 11 NOV 2017

Accepted 25 JAN 2018

Accepted article online 5 FEB 2018

Published online 24 FEB 2018

Abstract The validity of the sea ice rheological model formulated by Hibler (1979), which is widely used in present numerical sea ice models, is examined for the Sea of Okhotsk as an example of the seasonal ice zone (SIZ), based on satellite-derived sea ice velocity, concentration and thickness. Our focus was the formulation of the yield curve, the shape of which can be estimated from ice drift pattern based on the energy equation of deformation, while the strength of the ice cover that determines its magnitude was evaluated using ice concentration and thickness data. Ice drift was obtained with a grid spacing of 37.5 km from the AMSR-E 89 GHz brightness temperature using a maximum cross-correlation method. The ice thickness was obtained with a spatial resolution of 100 m from a regression of the PALSAR backscatter coefficients with ice thickness. To assess scale dependence, the ice drift data derived from a coastal radar covering a 70 km range in the southernmost Sea of Okhotsk were similarly analyzed. The results obtained were mostly consistent with Hibler's formulation that was based on the Arctic Ocean on both scales with no dependence on a time scale, and justify the treatment of sea ice as a plastic material, with an elliptical shaped yield curve to some extent. However, it also highlights the difficulty in parameterizing sub-grid scale ridging in the model because grid scale ice velocities reduce the deformation magnitude by half due to the large variation of the deformation field in the SIZ.

Plain Language Summary Sea ice plays an important role in shaping the polar climate. Therefore, it is quite important to accurately simulate its behavior in climate models. This study focuses on the treatment of the dynamical processes of sea ice in numerical models, especially the rheology relating ice stress to deformation. In these models, sea ice rheology is closely related to ice thickness. In many present models, the viscous-plastic rheology formulated by Hibler has been used, irrespective of region modeled and grid scales. In this study, the validity of this formulation was examined for the Sea of Okhotsk ice, a typical seasonal ice zone (SIZ), based on AMSR-derived ice drift and PALSAR-derived ice thickness, in comparison with the Beaufort Sea in the Arctic. The nearby coastal radar data were also used to assess scale dependence. Our observational results support the Hibler's formulation to some extent, suggesting its validity and applicability to the SIZ. However, it was also noted that the variation of the deformation field in the Sea of Okhotsk is so large that the deformation magnitude obtained on a grid scale is reduced by half, indicating the difficulty in parameterizing subgrid scale ridging in the model.

1. Introduction

Sea ice plays an important role in climate in the polar regions due to its higher albedo compared with surrounding seawater and its reduction or modulation of heat, moisture, and momentum exchange between the atmosphere and ocean. To predict the behavior of sea ice in global climate models, it is important to incorporate realistic dynamical processes such as ice motion and deformation caused by atmospheric, oceanic forcing, and the internal stress within sea ice pack. Therefore, sea ice rheology which relates sea ice stress to the large-scale deformation of the ice cover is an important component of numerical sea ice models (Feltham, 2008).

In many of the current sea ice models included in the climate simulations, the treatment of internal stress within sea ice area is based on the sea ice rheology formulated by Hibler (1979), in which sea ice behaves as a plastic material under the ordinary stress and as viscous fluid under subcritical stress (Hunke et al., 2010;

Losch et al., 2010; Wang, 2007). Although the Maxwell-Elasto-Brittle sea ice rheology has recently been shown to reproduce the fine features of sea ice near a strait successfully (Dansereau et al., 2017), it is not currently used in climate models. This concept was based on the isotropic and elastic-plastic approach of Coon et al. (1974), which was first identified during the Arctic Ice Dynamics Joint Experiment. The elastic behavior under subcritical stress in Coon et al. (1974) was replaced by viscous fluid to reduce the computational burden caused by the calculation of strain (Feltham, 2008). While many present numerical sea ice models adopt elastic-viscous-plastic rheology by Hunke and Dukowicz (1997) for computational efficiency and there are still debates of the efficient numerical implementation (Hibler & Vavrus, 2012), the basic concept of Hibler's rheology remains unchanged.

The Hibler (1979) formulation of rheology was initially developed to reproduce the seasonal variation of the perennial sea ice and thickness distribution in the Arctic Ocean. As for its applicability to the seasonal ice zones (SIZ), where mean floe sizes are smaller, it still needs evaluation from observational data. Since the treatment of the internal stress of sea ice floes is closely related to the ice thickening process due to deformation through ridging and rafting, this issue is important to the development of parameterization for predicting ice thickness distribution in the model. Given that the fraction of the SIZ in the Arctic Ocean is increasing in association with the recent rapid reduction of sea ice extent (e.g., Cavalieri & Parkinson, 2012; Stroeve et al., 2012), this utility of the Hibler (1979) rheology in the SIZ needs to be addressed.

Hibler's rheology assumes the following characteristics: (1) the whole sea ice area behaves like an isotropic and plastic matter under the ordinary stress, where the ice pack is always at the critical stress and in failure, and like a viscous fluid under the subcritical stress, (2) the yield curve is given by an ellipse with an aspect ratio of 2, and (3) ice strength is formulated as a function of ice concentration and thickness as follows:

$$P = P^* h \exp[-C(1-A)], \quad (1)$$

where A and h are the areal concentration and mass of thick ice within a grid cell (mean ice thickness is given by h/A), respectively, and P^* and C are fixed positive empirical constants. C is usually set to 20. Regarding (1), Hibler (1977) showed that for small strain rates, stochastic variations in sea ice deformation which is presumed to be plastic in nature can cause viscous behavior when averaged. Therefore, we focus on the treatment of sea ice as a plastic material in this study.

The validity of the yield curve for compacted pack ice has been investigated from several viewpoints, including the analysis of the horizontal deformation field, strain rates, and ridging from consideration of the energy balance (Fily & Rothrock, 1990; Rothrock, 1975; Stern et al., 1995) and the sensitivity of model representation of ice drift, area and thickness to different rheological formulations (e.g., Kreyscher et al., 2000; Miller et al., 2005; Wang, 2007; Zhang & Rothrock, 2005). The energy equation in Rothrock (1975) relates the energy sink due to the work done by ice interaction forces, such as ridging and sliding activities, to the total deformation field. We can evaluate this by considering if observed ice deformation follows that predicted (Stern et al., 1995; Thorndike et al., 1975; Ukita & Moritz, 1995; Wilchinsky & Feltham, 2004). Most previous studies inter-comparing model results tune the ice strength and yield curve shape by comparing model ice area, drift and thickness with observation. For example, other shapes of the yield curve, such as tear drop (Rothrock, 1975; Zhang & Rothrock, 2005), truncated ellipse (Geiger et al., 1998; Hibler & Schulson, 1997; Miller et al., 2005) and Mohr-Coulomb (Hibler, 2001; Hibler & Schulson, 2000; Hutchings et al., 2005; Ip et al., 1991), or changing the aspect ratio of the elliptical yield curve (Miller et al., 2005), have been examined in terms of how they improve model fit to observations. Since it is not easy to determine which yield curve is most appropriate just from observational data, we focus on evaluating the consistency of Hibler's rheology formulation especially for the yield curve.

The key to the evaluation of ice rheology from observational data is to obtain gridded data of ice concentration, velocity, and thickness distribution in the SIZ at a similar horizontal resolution to the numerical model for the same period. Recently, these data sets have become available with appropriate accuracy using satellite images and remote sensing data. This allows us to perform evaluations on scales appropriate for the SIZ. In this study, we focus on the Sea of Okhotsk in winter 2010, when the following comprehensive data sets were obtained. Ice drift was estimated from daily AMSR-E 89 GHz data using a maximum cross-correlation method with a grid spacing of 37.5 km (Kimura et al., 2013). To compare with the Arctic Ocean (following Stern et al., 1995), ice drift in the Beaufort Sea for the same period was analyzed in the same way. For ice concentration, a

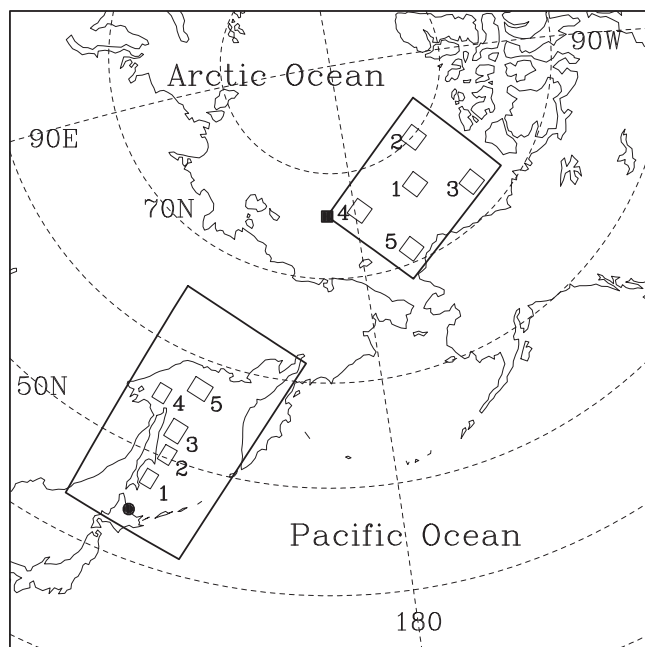


Figure 1. Geographical map showing the analysis areas in the Sea of Okhotsk and the Beaufort Sea. The squares (thin lines) within these seas denote the targeted areas for analysis. Each analysis area is numbered as shown. The solid circle in the southernmost Sea of Okhotsk denotes the position of the coastal radar, and the solid square of the Beaufort Sea denotes the origin of Figure 13. The periods for analysis were January–March 2010 for the numbered area in the Sea of Okhotsk and the Beaufort Sea, and January–April in 2003 for the coastal radar area.

product derived from AMSR-E 89 GHz with a grid spacing of 6.25 km, prepared by Bremen University, was used. Ice thickness was retrieved from the backscatter data of the Advanced Land Observing Satellite (ALOS)/Phased Array-type L-band SAR (PALSAR) with a grid spacing of 100 m, based on a field evaluation experiment being conducted in the same area (Toyota et al., 2011).

Furthermore, to examine scale dependence of our findings, coastal radar data obtained at Mombetsu (Figure 1), facing the Sea of Okhotsk, were used. The seaward-facing radar was operated remotely by Hokkaido University to monitor the sea ice area with a resolution of about 150 m and a range of about 70 km from the coast until 2004 (Ishikawa et al., 2004; Tabata, 1975). Although the radar data were normally obtained every three hours, we had an opportunity to operate it every 10 minutes on specific dates in winter 2003. With these data sets, ice drift patterns were calculated at a grid spacing of 1.3 km using a maximum cross-correlation method. While the ridging processes are controlled by the deformation field on scales greater than a few tens of kilometers, the actual ridging activities tend to occur on much smaller scales (~ 1 km). Although the period is different from that for the entire Sea of Okhotsk, the ice pack is similar between 2003 and 2010; maximum sea ice extent was 1.25×10^6 km² in 2003 and 1.11×10^6 km² in 2010, according to Japan Meteorological Agency, http://www.data.jma.go.jp/gmd/kaiyou/data/db/seaice/okhotsk/data/okhotsk_alldata.txt. Since the horizontal resolution is close to the scale of ridging processes, the coastal radar data set is expected to provide some useful information on the rheology related directly to them.

The validity of the Hibler (1979) rheology is investigated from a standpoint of whether observed horizontal strain rate of sea-ice follows relationships predicted by the theory of Rothrock (1975) of work done by deformation based on the strain energy equation. The central hypothesis is that the work needed to deform the material can be equated to the energy sinks in the ridging process. In analysis, we take a method following Fily and Rothrock (1990) and Stern et al. (1995), who examined the validity of Hibler's rheology, mainly for the Beaufort Sea by comparing the observed relative rates of divergence and shear rate with the theory derived assuming a specific shape of the yield curve. This method was adopted because it is simpler and more feasible than calculating the internal stress term of the momentum equation directly. While Stern et al. (1995) confirmed the consistency of the formulation to some extent, they did not evaluate the formulation of ice strength based on thickness because they paid more attention to the behavior of open water or leads. Also, this method has not yet been used to test the validity of a plastic rheology for the SIZ. In fact, to our knowledge, the formulation of P , equation (1), has never been tested against observation. Thus, our major questions in this paper are summarized as follows:

1. Is Hibler's formulation of rheology still valid in the Sea of Okhotsk, a typical SIZ, as well as in the Arctic Ocean?
2. If there are any differences between the two regions, what is the reason for that?
3. Does the validity of Hibler's formulation depend on horizontal and temporal scales?

We attempt to answer these questions with a comprehensive observational data set in this paper.

This paper is organized as follows: section 2 will describe the data sets we used and in section 3 we detail the background concepts and analytical methods used. Thereafter the results are shown in section 4 and then discussed in section 5.

2. Data

The study period for the Sea of Okhotsk analysis was primarily from January through March 2010, when comprehensive data sets of ice concentration, thickness distribution, and drift pattern were obtained. While

these three data sets (ice concentration, ice drift, and ice thickness) have different horizontal resolutions, the grid for ice drift data is chosen to synthesize them and the other data sets were adjusted to the ice drift data by taking the average within the grid cell. In addition, to examine the sea ice deformation field on smaller scales (~ 1 km), we also used coastal radar data from Mombetsu, located at the southernmost Sea of Okhotsk for the period of January–April 2003. The description of each data set is given in this section.

2.1. Ice Concentration

Sea ice concentration was obtained from the data set prepared by Bremen University (<http://www.iup.uni-bremen.de:8084/amsr/amsre.html>). This data set is based on the daily data of AMSR-E 89 GHz brightness temperature at both horizontal and vertical polarizations. Sea ice concentration was calculated using the ASI (ARTIST Sea Ice; ARTIST stands for Arctic Radiation and Turbulence Interaction Study) algorithm, providing a horizontal resolution in latitude and longitude of 6.25 km. This data set is described by Spreen et al. (2008).

2.2. Ice Drift

2.2.1. AMSR-E Imagery Data

The ice drift pattern was obtained by applying the maximum cross-correlation (MCC) method to successive satellite passive microwave (AMSR-E) imagery. The MCC method was first introduced and developed to automatically detect sea ice motion with successive visible Advanced Very High Resolution Radiometer (AVHRR) satellite imagery (Emery et al., 1991; Ninnis et al., 1986). This method calculates ice motion by correlating two sequential images and locating the area which has the maximum cross correlation between these images as the end points of the vectors in windowed portions of the images (Emery et al., 1991). This technique has also been applied to Synthetic Aperture Radar (SAR) (Collins & Emery, 1988; Fily & Rothrock, 1987) and Special Sensor Microwave Imager (SSM/I) data (Agnew et al., 1997; Kimura & Wakatsuchi, 2000; Kwok et al., 1998). The use of SSM/I has enabled the daily monitoring of ice drift pattern, irrespective of the weather conditions.

In this study, we used the daily AMSR-E 89 GHz brightness temperature data to obtain daily ice drift data on as small a scale as possible (https://nsidc.org/data/AE_S16), using the procedure described in Kimura et al. (2013). With a 6×6 -pixel array used for this procedure, sea ice drift data were obtained at a grid spacing of 37.5 km. The validity of this data set was examined by comparing with buoy position data from the International Arctic Buoy Programme in the Arctic Ocean and it was found that AMSR-E derived ice motion tends to slightly overestimate the ice velocity by 2.7–4.5% (Kimura et al., 2013) and the uncertainty is estimated to about 0.02 ms^{-1} (Sumata et al., 2015). Since the estimated bias is small, we do not take it into account in the following analysis.

2.2.2. Coastal Radar Data

The coastal radar was deployed at three stations located in the northeastern region of Hokkaido, Japan, to observe the detailed distribution of pack ice off the coast from 1967 to 1969, covering an area about 70 km wide and 250 km long with a wave frequency of 5.54 GHz (C-band) (Tabata, 1975). It normally operated every 3 hours during winter to record the sea ice conditions with a pixel size of 0.1 nautical mile (about 185 m) within 70 km of the station, until 2004 (Ishikawa et al., 2004). In winter 2003, a special opportunity existed at Mombetsu among these three stations to operate the radar every 10 minutes on 12, 13, and 23 February, 7, 8, 17, and 18 March, 8 and 9 April, to investigate the short-term variation of ice motion. With this 9 day data set, the ice drift was estimated from scenes obtained with a grid spacing of 1.3 km using a similar MCC method as applied to the AMSR-E imagery. As 10 minutes was too short to trace the ice displacement, 30 minutes was selected for the time interval of two sequential images and a 7×7 pixel array were used for calculating cross correlation.

2.3. Ice Thickness Data

Ice thickness data were obtained with a horizontal resolution of 100 m from PALSAR backscatter coefficients using an algorithm developed for the Sea of Okhotsk ice by Toyota et al. (2011). Here we describe the concept of this algorithm and evaluate the estimated ice thickness by comparing it with the ice growth estimated with the ERA-Interim meteorological reanalysis data.

2.3.1. Algorithm

The basic idea is that sea ice thickness growth in the SIZ is closely related to ridging activity (e.g., Toyota et al., 2007; Worby et al., 1996) and therefore surface roughness is expected to be a good indicator for

obtaining thickness distribution. PALSAR (L-band SAR) is useful for detecting rough surfaces because the backscatter coefficient of SAR is sensitive to the surface roughness larger than the wavelength (Massom, 2006) and the wavelength of PALSAR (0.24 m) is close to the surface roughness of deformed ice in this region (> 0.2 m; see Figure 3 of Toyota et al., 2011). This idea was supported by an air-borne Polarimetric and Interferometric Synthetic Aperture Radar (Pi-SAR) and the space-borne PALSAR evaluation experiments in the Sea of Okhotsk (Toyota et al., 2009, 2011). In-situ observations of ice thickness were used to develop a thickness retrieval method for PALSAR. The regression to retrieve ice thickness was estimated as

$$H_i = 0.047 \times BS + 1.012 \quad (\text{for } -14.2 < BS < -9.6 \text{ dB}) \quad (2)$$

where H_i is ice thickness in meters and BS is backscatter coefficient in dB with a pixel size of 100 m at HH polarization in a ScanSAR mode normalized to an incident angle of 30.4 degrees at the center of the image. Since the data range of equation (2) is relatively narrow, we need evaluation to apply to this analysis. Note that the thickness for this regression was measured with a video system (Toyota et al., 2004), which means that significantly ridged ice was excluded from thickness measurement.

From January–March 2010, PALSAR images covering the whole southern Sea of Okhotsk were obtained approximately once a week through the contract between the Japan Aerospace Exploration Agency (JAXA) and Japan Coast Guard for the prevention of ship disasters. The temporal evolution of the PALSAR-derived ice thickness for the period of 7 January to 6 March 2010 is depicted in Figure 2. In this figure, sea ice area is extracted as that with ice concentration greater than 15%. It is shown that overall ice thickness increased from about 0.2 m in January to 0.4–0.5 m in March, although abrupt changes sometimes occur that are likely due to large-scale deformation and pile-ups caused by short-term variability of ice drift patterns.

2.3.2. Evaluation

We evaluate the PALSAR-derived ice thickness by comparing it with the temporal evolution of thermodynamic ice growth calculated with the ERA-Interim data set (1.5 deg \times 1.5 deg). While this method appears to be inconsistent with the concept of the thickness algorithm based on a deformation process, our idea is as follows: if a deformation process occurs, local ice thickness might deviate from the thermodynamic growth amount. In such case, the ice volume produced within a finite area (0.2 deg \times 0.2 deg) would coincide roughly with thermodynamic ice growth because thermodynamic ice growth is quite limited, even in winter due to the abundant solar radiation in this region (Toyota & Wakatsuchi, 2001). Therefore, when averaged within a finite area, ice thickness would be comparable with the thermodynamic ice growth. It should be noted that when a large-scale convergence occurs over the whole finite area, the derived thickness may deviate much from the thermodynamic ice growth.

Ice growth rate was estimated using the ERA-Interim data set with a 1-D thermodynamic ice model similar to that of Maykut (1982), including surface air pressure, air temperature, dew point temperature, wind speed, and cloud amount, 4 times per day (03, 09, 15, 21 Japan Standard Time). Solar radiation was determined by the empirical formula of Kim (1992) and downward long wave radiation flux was calculated from the empirical formula of Maykut and Church (1973). We assumed that ocean heat flux is negligible because the water temperature in the surface mixing layer, extending to ~ 30 m depth, was shown to be nearly at the freezing point through the CTD and XBT measurement in this region. Snow depth was assumed to be one fifth of ice thickness based on the observational result (Toyota et al., 2000). The amount of ice growth was calculated at the grid points of P1 (48°N 144°E), P2 (46.5°N 144°E), and P3 (45°N 144°E) in Figure 2. Calculation began when the sea ice cover extended southward to each grid point, as judged from the AMSR-E sea ice concentration map. Observational data recorded on the ship around in the area (44.4 – 45.5 °N, 142.1 – 144.6 °E) during the period of 5–9 February 2010 showed that ERA-Interim data set at P3 accurately reproduced the real meteorological conditions with a root mean square error of 2.0 hPa for sea level pressure, 1.5°C for air temperature, and 3.8 m/s for wind speed. We confirmed that the error of the ERA-Interim data set results in the predicted ice thickness of ± 1 cm at most.

The time series of calculated ice thicknesses at P1, P2, and P3 are shown in Figure 3 and are compared with PALSAR-derived ice thickness. The data points and error bar of each plot corresponds to mean and a standard deviation of ice thickness within a 0.2 deg \times 0.2 deg area, where about 33,000 PALSAR pixels are contained, surrounding each point. Figure 3 shows that the PALSAR-derived ice thickness is approximately consistent with thermodynamic ice growth except at P1, where the ice was kept thin by the strong off shore

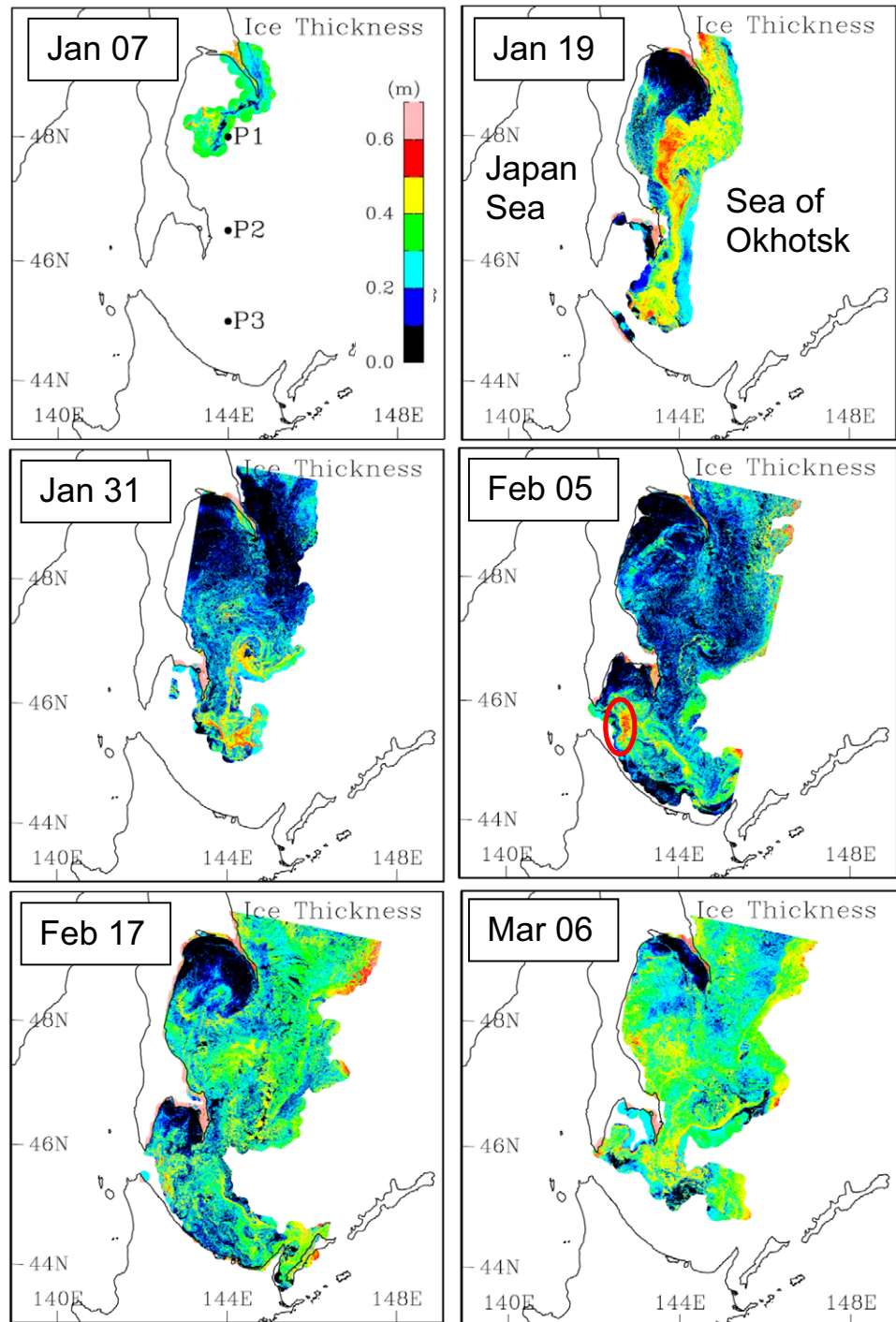


Figure 2. Temporal evolution of the PALSAR-derived ice thickness in the Sea of Okhotsk from January to March 2010. Sea ice area is extracted for ice concentration larger than 15%. The red circle on 5 February denotes the region where pancake ice was dominant (see Figure 4a for the photo.) "P1," "P2," and "P3" on 7 January are the ERA-Interim grids, where thermodynamic growth was calculated for evaluation (Figure 3).

winds. Even at P1, the fact that the initial ice growth amount of 0.14 m almost coincides with PALSAR-derived ice thickness of 0.13 m on 12 January may justify the validity of equation (2). Significant deviations occurred abruptly at P2 and P3 on some days (e.g., see arrows in Figure 3). Since the AMSR-E derived ice drift patterns showed a large-scale convergence on these days, it is likely that the abrupt increase (decrease)

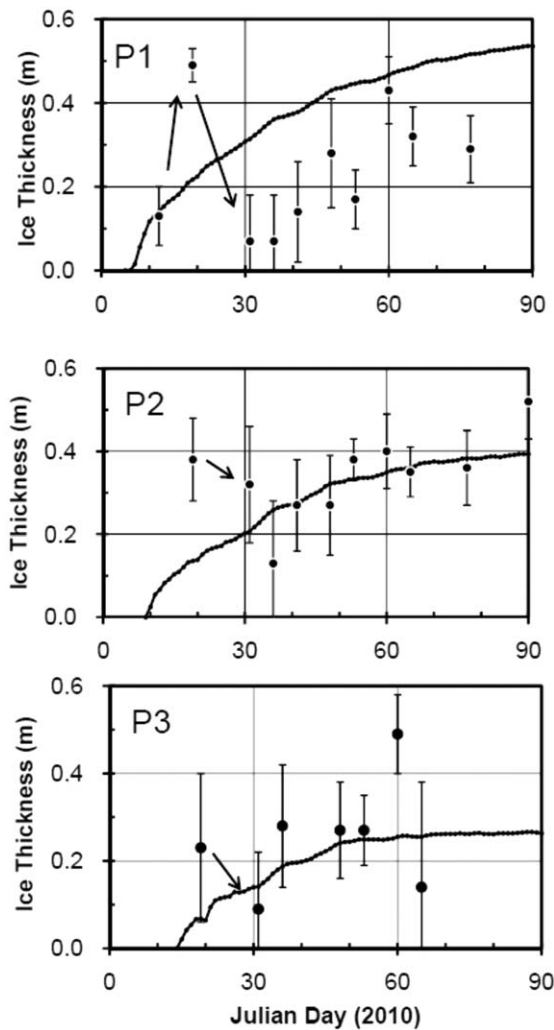


Figure 3. Comparison between thermodynamic growth (solid line) and PAL-SAR-derived ice thickness (solid circles with error bars) at 3 locations P1–P3 (see Figure 2 (first panel) for locations). Solid circles and error bars denote mean and a standard deviation of ice thickness, respectively, within a 0.2×0.2 deg area surrounding each grid point. The arrows in the figures denote the abrupt change of ice thickness.

of ice thickness was caused by ridging (disintegration) activities of sea ice on a scale larger than the $0.2 \text{ deg} \times 0.2 \text{ deg}$ area.

Pancake ice is another factor which can affect the thickness algorithm. Although the thickness of pancake ice is mostly less than 15 cm, the raised rim of this ice type tends to return large L-band SAR backscatter coefficients. This is confirmed by the fact that the backscatter coefficient showed significantly high values (a red circle in Figure 2) on 5 February when such pancake ice area was vast (Figure 4a). Therefore, we should be careful when analyzing the sea ice thickness in the marginal ice zone where pancake ice with significantly raised rim sometimes appears. However, considering that such vast pancake ice area is relatively limited in the southern Sea of Okhotsk, we conclude that L-band SAR is useful for the estimation of ice thickness in this region.

3. Methods

Here we briefly describe the background theory of Rothrock (1975) that we follow in this study. Given the hypothesis that the total work rate per unit area done by large-scale stress can be equated to the energy sinks in the ridging process, the energy equation is described as follows:

$$\sigma_I \dot{\epsilon}_I + \sigma_{II} \dot{\epsilon}_{II} = |\dot{\epsilon}| \alpha_r(\theta) P \quad (3)$$

where σ_I and σ_{II} denote the mean normal stress and maximum shear stress, respectively, and are described in terms of the principal stresses σ_1 and σ_2 as:

$$\sigma_I = (\sigma_1 + \sigma_2)/2, \sigma_{II} = (\sigma_1 - \sigma_2)/2 \quad (4)$$

The strain rate invariants $\dot{\epsilon}_I$ and $\dot{\epsilon}_{II}$ are the velocity divergence and maximum shear strain rate, respectively, and are described in terms of the principal strain rates $\dot{\epsilon}_1$ and $\dot{\epsilon}_2$ as $\dot{\epsilon}_I = \dot{\epsilon}_1 + \dot{\epsilon}_2$ and $\dot{\epsilon}_{II} = \dot{\epsilon}_1 - \dot{\epsilon}_2$ ($\dot{\epsilon}_1 > \dot{\epsilon}_2$). They are described explicitly in terms of the velocity derivatives as follows (Thorndike, 1986):

$$\dot{\epsilon}_I = \frac{\partial u}{\partial x} + \frac{\partial v}{\partial y}, \dot{\epsilon}_{II} = \sqrt{\left(\frac{\partial u}{\partial x} - \frac{\partial v}{\partial y}\right)^2 + \left(\frac{\partial u}{\partial y} + \frac{\partial v}{\partial x}\right)^2} \quad (5)$$

$|\dot{\epsilon}|$ and θ are polar coordinates in the $\dot{\epsilon}_I$ – $\dot{\epsilon}_{II}$ plane and described as:

$$|\dot{\epsilon}| = \sqrt{\dot{\epsilon}_I^2 + \dot{\epsilon}_{II}^2}, \theta = \tan^{-1}(\dot{\epsilon}_{II}/\dot{\epsilon}_I) \quad (6)$$

showing the magnitude of the deformation rate and the relative amount of divergence and shear, respectively. The coefficient $\alpha_r(\theta)$ is a measure of the relative rate of divergence (Thorndike et al., 1975), taking the values of zero for $\theta=0$ and unity for $\theta=\pi$. P is the strength of the ice pack in compression. Thus, the left-hand side of equation (3) corresponds to the rate of plastic work done by deforming the sea ice area. On the other hand, the right-hand side of equation (3) is related to the redistribution function ψ in the equation for the thickness distribution of Thorndike et al. (1975). It represents the energy sinks in the ridging processes, including the rates of potential energy production and frictional energy loss combined in the factor P . The approach of equation (3) was generalized by including the additional energy sink due to sliding motion of floes parallel to cracks (Feltham, 2008; Moritz & Ukita, 2000; Ukita & Moritz, 1995). However, this effect was not considered here because floe sizes are mostly smaller than a few hundreds of meters in the Sea of Okhotsk (Figure 4b; Toyota et al., 2007) and therefore it seems unlikely that sliding affects the dynamics significantly.

Based on equation (3) and the assumption that the ice cover is isotropic, Rothrock (1975) showed that $\alpha_r(\theta)$ is uniquely related to the shape of the yield curve by applying the normal flow rule. Considering the requirement that the yield curve be convex and that tensile stress never occurs, he postulated the shape of

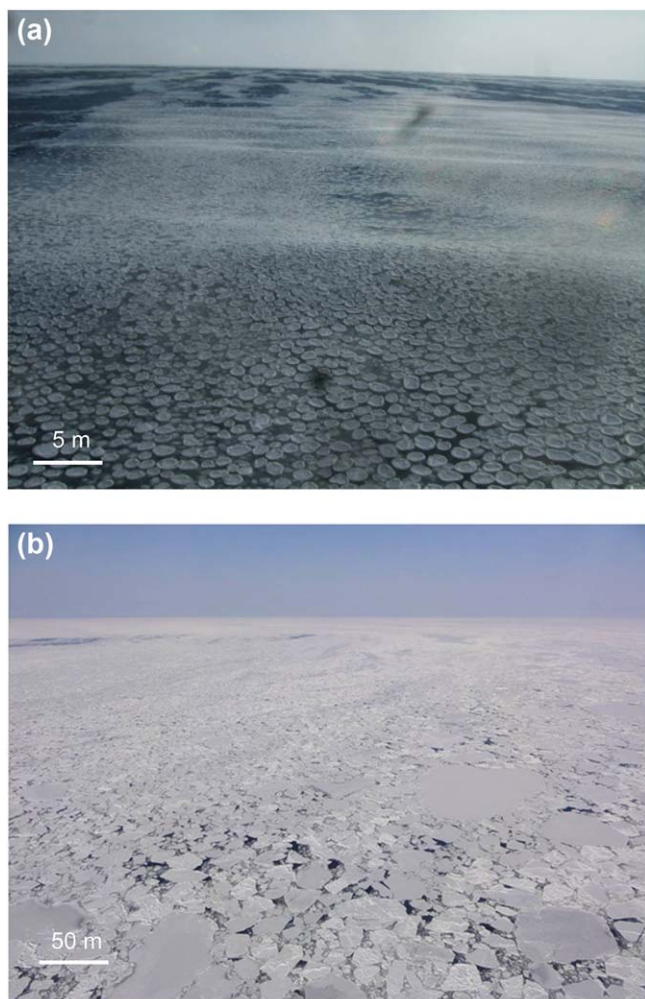


Figure 4. Oblique photographs of the sea ice conditions in the Sea of Okhotsk, showing (a) widespread pancake area taken from the P/V Soya on 5 February 2010 within the red circle region of Figure 2. The width of the photo is approximately 50 m. (b) Typical ice floes taken from a helicopter at an altitude of 300 m around N45 E144 on 15 February 2011. The width of the photo is approximately 500 m.

the yield curve to be like a tear drop or parabolic lens. Yet, it seems worthwhile to consider what kind of yield curve a plastic material obeys in general because the treatment of sea ice area as a plastic material has been widely accepted since Coon (1974) first presented it (Leppäranta, 2005). The plasticity theory states that plastic deformation occurs when the shear stress reaches a critical value unique to the material, and the yield criterion for a 3-D material is provided in the principal stress deviator components as follows (Kachanov, 1971): per the Tresca-Saint Venant criterion, yielding occurs when at least one of equation (7) holds.

$$|\sigma_2 - \sigma_3| = 2k, |\sigma_3 - \sigma_1| = 2k, |\sigma_1 - \sigma_2| = 2k \quad (7)$$

where k is the maximum tangential stress.

Von Mises presented equation (8) to avoid the mathematical singularity in treating equation (7).

$$(\sigma_1 - \sigma_2)^2 + (\sigma_2 - \sigma_3)^2 + (\sigma_3 - \sigma_1)^2 = 8k^2 \quad (8)$$

For the plane stress, $\sigma_3 = 0$ is substituted to these equations, and then equations (9) and (10) can be derived:

$$\text{Tresca-Saint Venant criterion : } \sigma_1 = \pm 2k, \sigma_2 = \pm 2k, \sigma_1 - \sigma_2 = \pm 2k \quad (9)$$

$$\text{Von Mises criterion : } \sigma_1^2 - \sigma_1\sigma_2 + \sigma_2^2 = 4k^2 \quad (10)$$

The yield curves designated by these two equations are drawn in Figure 5a. As shown in the figure, equation (9) corresponds to a symmetric hexagon with an aspect ratio of 2, while equation (10) to the ellipse with an aspect ratio of $\sqrt{3}$. In terms of σ_I and σ_{II} , equation (10) becomes

$$\left(\frac{\sigma_I}{2k}\right)^2 + \left(\frac{\sigma_{II}}{2k/\sqrt{3}}\right)^2 = 1. \quad (11)$$

It is found that these figures are close to Hibler's formulation of the yield curve (Figure 5b) for the stress deviator which is obtained by subtracting the mean normal stress ($=P/2$) from σ_1 and σ_2 . Therefore, if we set a yield curve as the ellipse with an aspect ratio of e and e is confirmed to be about $\sqrt{3} \sim 2$, it would support the choice of a failure criteria similar to Von Mises or Tresca, which Hibler (1979) approximates. Following the

method of Rothrock (1975), the elliptical yield curve with an aspect ratio of e provides $\alpha_r(\theta)$ in the form of equation (12) (Stern et al., 1995):

$$\alpha_r(\theta) = -\frac{1}{2} \cos \theta + \frac{1}{2} \sqrt{\cos^2 \theta + \sin^2 \theta / e^2}. \quad (12)$$

Here we tried to evaluate the shape of yield curve by comparing $\alpha_r(\theta)$ between observation and theory.

Next, we explain how to estimate $\alpha_r(\theta)$ from observation. Basically, we followed the method of Stern et al. (1995) in which the coefficient $\alpha_0(\theta)$ ($=\cos \theta + \alpha_r(\theta)$), a measure of the relative rate of opening, was estimated with $\alpha_r(\theta)$ for the Beaufort Sea using SAR-derived ice drift data on a regular 5 km grid. With the area-averaged partial derivatives of displacement for three days within the total area of one SAR image (about 100 km scale), they calculated ε_I and ε_{II} , and then the magnitude of deformation ($|\varepsilon|$). The opening (closing) amount was calculated by summing up the positive (negative) values of divergence at each grid cell for the total area. By dividing the calculated opening (closing) amount by $|\varepsilon|$, they could obtain $\alpha_o(\theta)$ ($\alpha_r(\theta)$). The concept of this method originates from Thorndike (1986). In our case, we calculated the closing rate by summing up the negative values of divergence at each grid cell for the whole targeted area, set to about 150 km for the AMSR-derived ice drift data and about 10–30 km for the coastal radar-derived ice drift data.

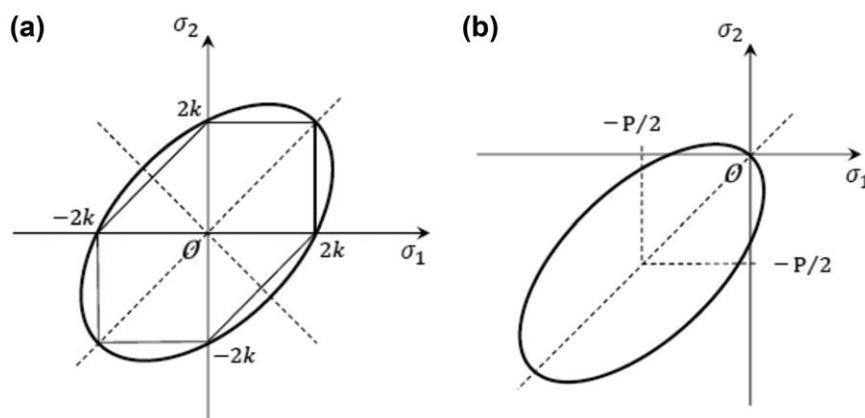


Figure 5. Yield criteria for plane stress in the σ_1 - σ_2 plane, formulated by (a) The Tresca-Saint Venant (a hexagon with an aspect ratio of 2 drawn with a thin solid line) and Von Mises (an ellipse with an aspect ratio of $\sqrt{3}$ drawn with a thick solid line) for a plastic material. (b) Hibler (1979) (an ellipse with an aspect ratio of 2) for the viscous-plastic rheology of sea ice area. k and P denote the maximum tangential stress and the strength of the ice cover, respectively. Note that the aspect ratio of each figure is approximately 2.

Practically, the whole targeted area corresponds to a unit grid cell in the numerical model, while each grid cell of the drift data corresponds to sub-grid scale in the model at which local convergence associated with ridging occurs. Thus, our analysis is closely related to the problem of parameterization in the numerical model. We can evaluate the optimal value of e by plotting α_r as a function of θ and comparing it with the theoretical relationship between these, equation (12).

Another characteristic of Hibler’s formulation is that the strength of the ice pack P in equation (3) was given as a function of A and h (equation (1)). For the targeted region in the Sea of Okhotsk, we can calculate A and h from the satellite data sets and $|\dot{\epsilon}|$ from the ice drift pattern. Thus, if we set $C = 20.0$ and $P^* = 5.0 \times 10^3 \text{ Nm}^{-1}$ in equation (1), following Hibler (1979), the right-hand side of equation (3) can be estimated. Since this term corresponds to the energy sinks due to ridging, it is expected that the higher it becomes, the more the mean ice thickness increases. Therefore, it would be possible to evaluate the formulation of equation (1) by comparing the real ice thickness change with the right-hand side of equation (3). Although there is much uncertainty in P^* , since it is a linear factor, it would be possible to check at least the consistency of the function P and the concept of equation (3) by examining the correlation between these two factors.

The horizontal variation of the deformation field can be examined from consideration of the strain ellipse at each grid cell. The strain ellipse is a 2-D graphical representation (i.e., phase-space) to visualize the amount of linear and angular strain involved in the deformation by showing how a circle of unit radius is deformed into an ellipse with two axes related to the principal strain rate components. The strain ellipse is defined by the dimensions and orientation of the long and short principal strain axes. The lengths of the long and short principal strain axes are $1 + \dot{\epsilon}_1$ and $1 + \dot{\epsilon}_2$, respectively. The orientation of the principal strain axes (φ) is calculated with the following equation:

$$\tan(2\varphi) = \frac{2\dot{\epsilon}_{xy}}{\dot{\epsilon}_{xx} - \dot{\epsilon}_{yy}} \tag{13}$$

where $\dot{\epsilon}_{xx} = \partial u / \partial x$, $\dot{\epsilon}_{yy} = \partial v / \partial y$, and $\dot{\epsilon}_{xy} = (\partial u / \partial y + \partial v / \partial x) / 2$. One example is shown in Figure 6. Since the change in area of the strain ellipse from the original circle is equal to $\pi(\dot{\epsilon}_1 + \dot{\epsilon}_2)$, it indicates the degree of divergence. Thus, the alignment of the strain ellipse estimated at each grid cell is expected to visually show the horizontal variation of the deformation field.

4. Results

We will first present our results about the shape of the yield curve deduced from the deformation field based on AMSR-E derived ice drift for the Sea of Okhotsk and the Beaufort Sea, and coastal radar derived ice drift for the southernmost Sea of Okhotsk. Then the result about the formulation of P will be shown.

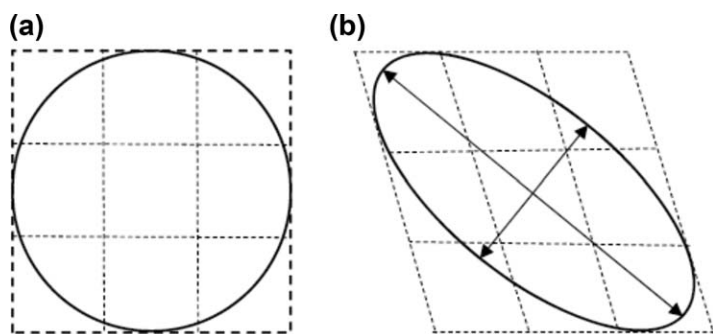


Figure 6. Schematic picture of a strain ellipse, explaining how the original circle (a) is distorted into an ellipse (b) under the stress. The two axes of the ellipse are expressed by $1+\hat{\epsilon}_1$ and $1+\hat{\epsilon}_2$ using the principal strain rates. φ is the rotation angle of the principal axes from the original direction.

4.1. The Shape of Yield Curve Deduced From Deformation Field

4.1.1. Large Scale

4.1.1.1. Sea of Okhotsk

Sea ice area in the Sea of Okhotsk is significantly variable on both inter-annual and seasonal time scales (Ohshima et al., 2006), making it important to carefully choose areas for analysis that are suitably representative. Thus, we focus on several fixed areas where the sea ice drift pattern is characteristic of the broader region. Five areas were selected for analysis based on the monthly mean ice drift divergence in February 2010 (Figure 7a). Areas 1, 2, and 4 (shown in Figure 7b) are on average convergent, and Areas 3 and 5 are divergent. Each is composed of 4×5 (Area 1), 4×5 (Area 2), 5×6 (Area 3), 4×5 (Area 4), and 6×5 (Area 5) grid cells, corresponding to about $150\sim 200$ km square. To examine the potential for parametrization, the areas were defined to be comparable to the grid size of coarse numerical sea-ice models and to contain as many grid cells as possible.

To begin with, we followed, exactly, the method of Stern et al. (1995) to calculate $\alpha_r(\theta)$: i.e., we first calculated the area-averaged spatial derivatives of ice velocity for each targeted area using the daily ice drift data sets, and then derived each component of the strain rate tensor $\dot{\epsilon}_{ij}$ from these data to obtain the magnitude of the deformation $|\dot{\epsilon}|$. This is essentially a strain rate calculated from the regional averaged velocity. The closing amount was calculated by summing up only the negative values of divergence at each grid cell within the individual targeted areas, and $\alpha_r(\theta)$ was estimated by dividing total closing by $|\dot{\epsilon}|$ for each area. This calculation is performed for each day. Thus, daily values of $\alpha_r(\theta)$ were obtained for each targeted area. The result is shown in Figure 8, where $\alpha_r(\theta)$ is plotted as a function of θ , together with the theoretical lines that obey equation (12) for $e=1, 2$, and ∞ , corresponding to the values proposed by Thorndike et al. (1975), Hibler (1979), and Flato and Hibler (1992), respectively. In particular, $e=\infty$ means that the large scale shear strain rate never contributes to the convergence rate on smaller scales (i.e., α_r becomes zero for θ less than 90 deg). To reduce the error due to the measurement accuracy, only the data with a relatively large

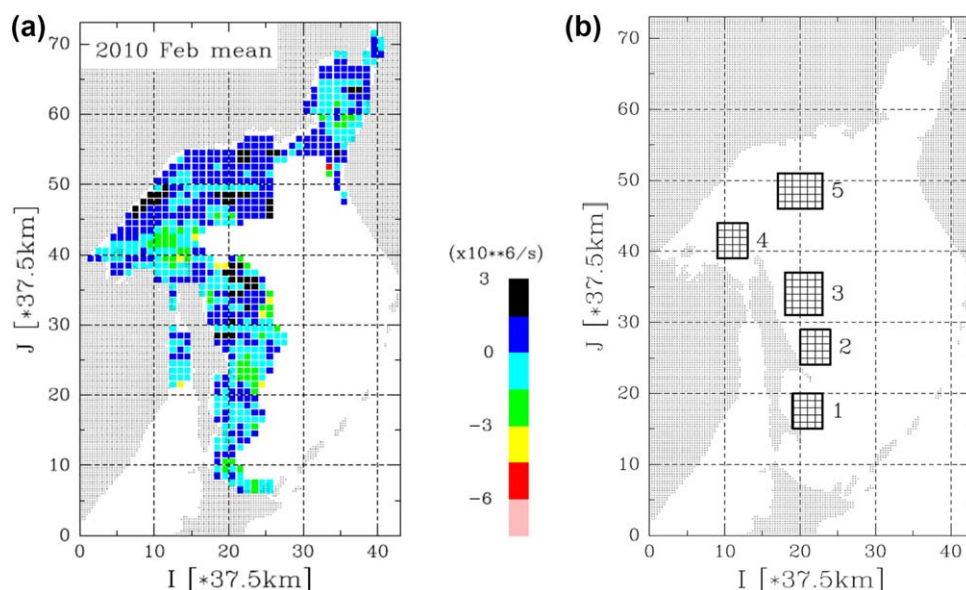


Figure 7. Targeted areas for analysis in the Sea of Okhotsk, selected based on (a) Distribution of mean ice velocity divergence in February 2010. (b) Five targeted areas. To explicitly show the horizontal scale, the x-y coordinate, expressed by distance from the origin was used instead of longitude and latitude. Note that Areas 1, 2, and 4 corresponds to relatively convergent areas, while Areas 3 and 5 to relatively divergent areas. The horizontal and vertical lines within each area represent the grid cells of the ice drift data set with a spacing of 37.5 km.

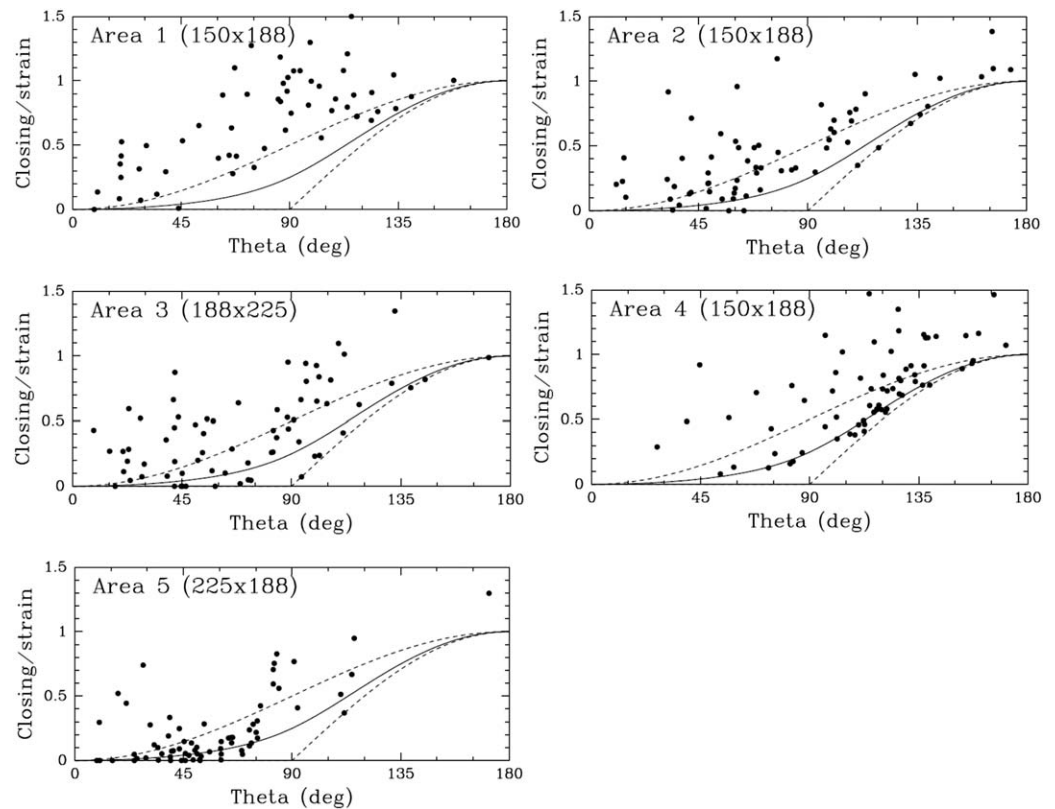


Figure 8. Closing amount/ $|\dot{\epsilon}|$, expressed by α_r plotted as a function of daily θ for each area in the Sea of Okhotsk. The period for analysis is January–March 2010 for all areas. The size of each area is shown in the parenthesis in km^2 . The plots are limited to the data with $|\dot{\epsilon}| \geq 0.1 \text{ d}^{-1}$. Note that $|\dot{\epsilon}|$ was calculated from the area-averaged spatial derivatives $\langle \partial u_i / \partial x_j \rangle$. Theoretical lines of α_r for elliptical yield curves with aspect ratios of 1 (upper broken line), 2 (solid line), and ∞ (lower broken line) are also drawn.

strain rate ($|\dot{\epsilon}| \geq 0.1 \text{ d}^{-1}$, derived from $\Delta u_i / \Delta x_j \sim 0.04 \text{ ms}^{-1} / 37.5 \text{ km}$) are plotted, taking into account that the ice drift error of this data set is estimated to be about 0.02 ms^{-1} (Sumata et al., 2015).

It is clear from Figure 8 that the observed α_r deviates significantly from all of the theoretical solutions, which are bounded by $e = 1$ to ∞ . Even if the data are limited to a larger deformation rate ($|\dot{\epsilon}| \geq 0.3 \text{ d}^{-1}$), the observed result was not greatly improved despite the higher values of α_r being eliminated (not shown). This means that it is difficult to estimate the local scale convergence (\sim a few tens of km) just from the larger scale (\sim a few hundreds of km) drift pattern. That several α_r values exceed unity in Figure 8 is probably attributable to an underestimation of $|\dot{\epsilon}|$ because the spatial derivatives of the ice velocity are flattened when calculating the average. To demonstrate this, we examined the distribution of the strain ellipse on each day within the targeted areas. One example is shown in Figure 9. Figure 9a shows the ice drift pattern with ice concentration on 19 February 2010, when the ice drift in the Sea of Okhotsk showed a systematic pattern on a large scale with relatively high velocities ($\geq \sim 0.5 \text{ ms}^{-1}$). Figures 9b, 9d, and 9f show the distributions of the strain ellipses within Area 1, 3, and 5, respectively. For comparison, the strain ellipses for the combined areas, obtained using the area-averaged strain rate components, are also shown in Figure 9c (Area 1), Figure 9e (Area 3), and Figure 9g (Area 5). Of highest relevance, the horizontal variation of strain ellipse is so large for all of the targeted areas that the area-averaged strain ellipse does not represent the small-scale deformation rate at all. The results were comparable to those found on the other days of analysis.

To ensure the mean strain rate is correctly estimated, we attempted to calculate the principal strain rates from the components of divergence $\dot{\epsilon}_I$ and shear $\dot{\epsilon}_{II}$ calculated at each grid cell. By taking the averages of $\dot{\epsilon}_I$ and $\dot{\epsilon}_{II}$ within the targeted areas, we can estimate the area-averaged divergence $\langle \dot{\epsilon}_I \rangle$ and shear $\langle \dot{\epsilon}_{II} \rangle$ components without flattening the spatial derivatives of the ice drift pattern. As such, $|\dot{\epsilon}|$ was derived from

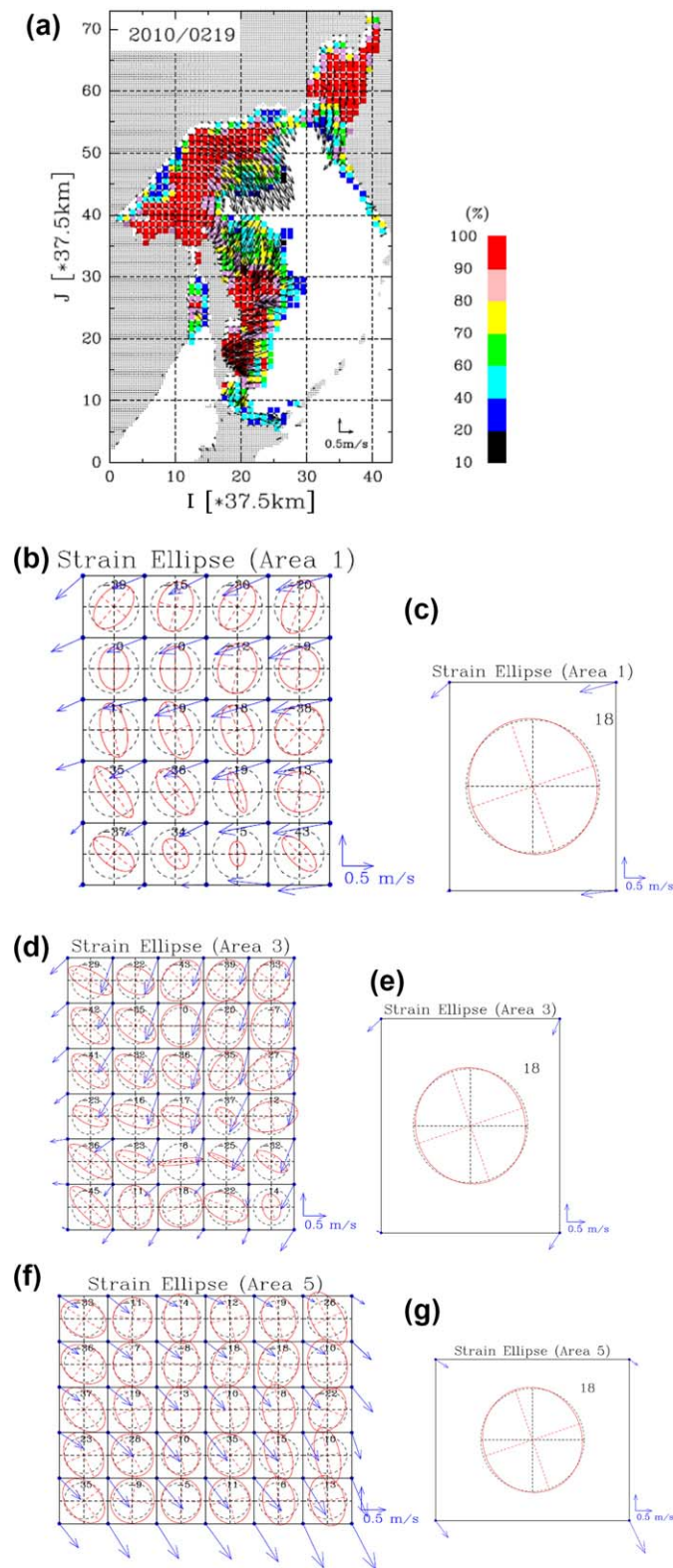


Figure 9. Characteristics of the deformation field in the Sea of Okhotsk on 19 February 2010. (a) Ice drift pattern with ice concentration Strain ellipse within Area 1 with ice velocity (blue arrows) and the value of ϕ , the orientation of the principal strain axes (degrees), shown for (b) each grid cell and (c) the area mean. (d) Same as Figure 9b except for Area 3 (e) Same as Figure 9c except for Area 3 (f) Same as Figure 9b except for Area 5 (g) Same as Figure 9c except for Area 5. Note the large variation of strain and the difference between area mean and individual ellipses at each grid cell.

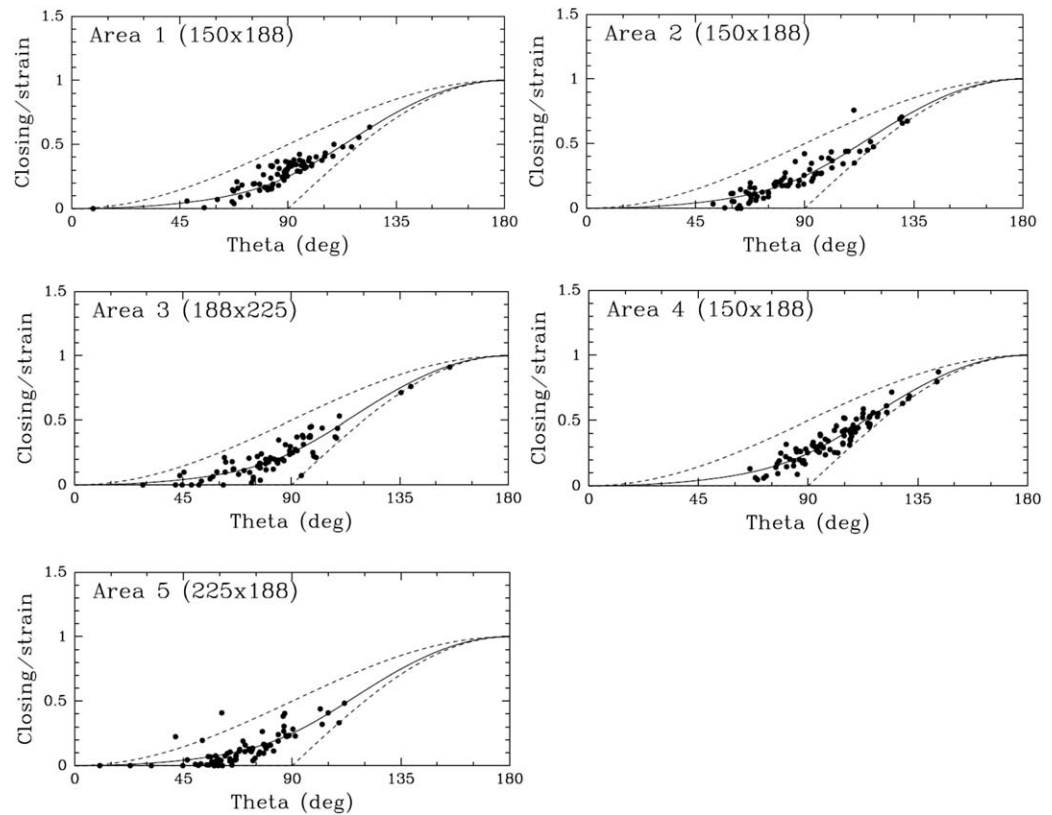


Figure 10. Same as Figure 8 except that $|\dot{\epsilon}|$ was calculated using the area-averaged divergence $\langle \dot{\epsilon}_I \rangle$ and shear $\langle \dot{\epsilon}_{II} \rangle$ for each area in the Sea of Okhotsk.

$\sqrt{\langle \dot{\epsilon}_I \rangle^2 + \langle \dot{\epsilon}_{II} \rangle^2}$. The remainder of the calculation was unchanged. The obtained α_r are plotted as a function of θ in Figure 10. With this corrected calculation method, mean $|\dot{\epsilon}|$ increased significantly by about a factor of 2 (Table 1). No data were excluded from the plot when the same threshold ($|\dot{\epsilon}| \geq 0.1 d^{-1}$) was applied. We found that α_r calculated from observation with our corrected method is in good agreement with the theoretical line for $e=2$ for all the targeted areas. Reflecting the characteristic drift pattern in each targeted area, the plots are somewhat biased to $\theta > 90$ deg (convergence) in Area 1, 2, and 4, and biased to $\theta < 90$ deg (divergence) in Area 3 and 5. Nevertheless, it is interesting that in both cases the data are close to the theoretical line of $e=2$. In particular, it should be noted that even for pure shear ($\theta=90$ deg), α_r is not zero but takes a value of 0.25. This means that pure shear on a large scale can contribute to local-scale convergence and thereby ridging.

Table 1
Temporal Averages of the Magnitude of Strain Rate for the Analysis Period With Optimal e

	Sea of Okhotsk			Beaufort Sea		
	Method 1	Method 2	e	Method 1	Method 2	e
Area 1	0.19 ± 0.14 (77)	0.49 ± 0.13 (77)	1.7	0.09 ± 0.06 (87)	0.12 ± 0.06 (90)	2.6
Area 2	0.28 ± 0.20 (72)	0.50 ± 0.18 (72)	2.0	0.07 ± 0.04 (87)	0.11 ± 0.05 (89)	2.2
Area 3	0.19 ± 0.14 (77)	0.57 ± 0.16 (76)	2.0	0.18 ± 0.09 (83)	0.14 ± 0.07 (87)	2.9
Area 4	0.20 ± 0.11 (86)	0.38 ± 0.17 (86)	2.0	0.09 ± 0.06 (79)	0.12 ± 0.06 (88)	2.5
Area 5	0.27 ± 0.15 (77)	0.42 ± 0.19 (77)	2.0	0.15 ± 0.09 (82)	0.22 ± 0.15 (89)	3.0
Mean	0.23 ± 0.05	0.47 ± 0.07	1.9	0.12 ± 0.05	0.14 ± 0.04	2.6

Note. In the table, mean ± one standard deviation is listed for each area. Method 1 is to calculate the magnitude from area-averaged spatial derivatives of ice velocity, while Method 2 from area-averaged divergence and maximum shear rate. The number in parenthesis denote the number of data points. The unit of strain rate magnitude is d^{-1} . Optimal e was obtained in Method 2 using the least square fit.

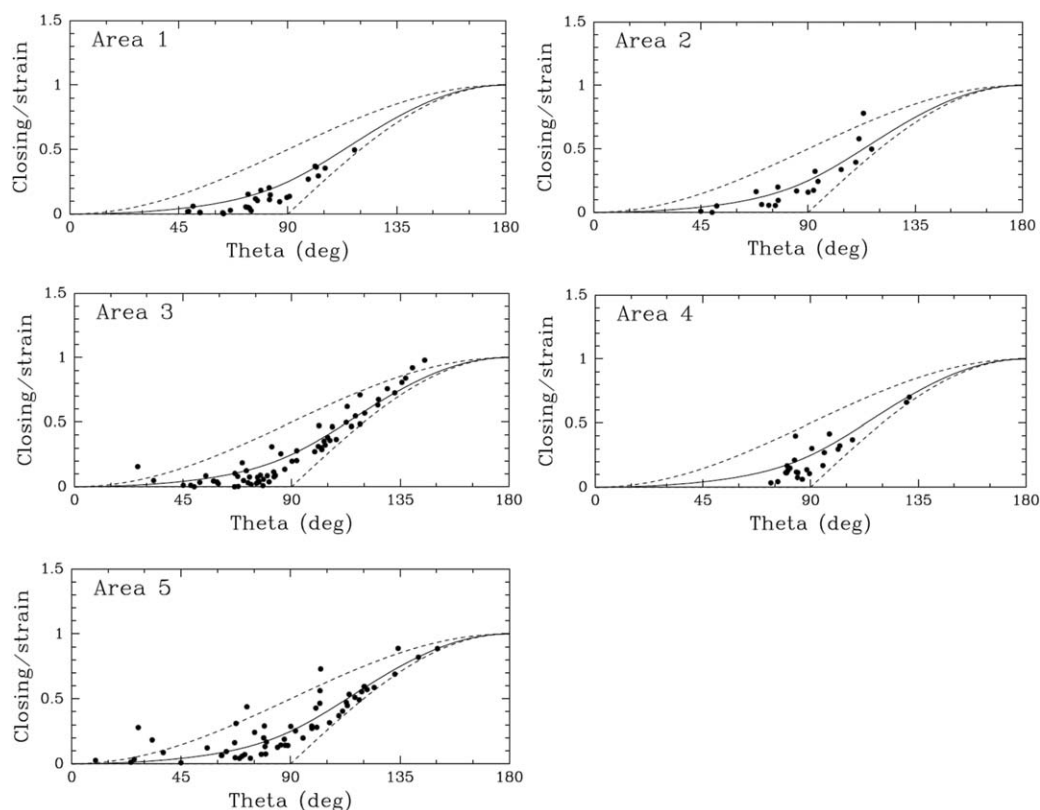


Figure 11. Same as Figure 8 except for the Beaufort Sea. The size of each area is all $188 \times 188 \text{ km}^2$.

To estimate the optimal value of e , the mean square error from the theoretical line was plotted as a function of e . The result shows that the optimal value of e is 1.7 for Area 1 and 2.0 for Area 2–5, close to the criterions of Tresca–Saint Venant or Von Mises in all 5 areas. In addition, the observational data have sufficiently positive values of α_r , even for $\theta < 90$ deg, to suggest that in the Sea of Okhotsk an ellipse may be a more appropriate yield curve shape than the tear-drop or lens shape that would have smaller values of α_r for $\theta < 90$ deg (see Figures 6 and 7 of Rothrock, 1975). These results are consistent with the concept of treating sea ice as a plastic material and the formulation of Hibler’s rheology.

However, specific to scale and, in particular, the decision making involved in a model grid size, it should be kept in mind that α_r calculated from the area-averaged (about $200 \times 200 \text{ km}^2$) spatial derivatives of ice drift deviated significantly from the theoretically predicted values, which are bounded by $e = 1$ to ∞ . Our analysis showed that this significant deviation resulted from the underestimation of $|\dot{\epsilon}|$ approximately by half (Table 1), caused by the large variation of the deformation field. This indicates it is not possible to parameterize the local scale (about 40 km) deformation field with a grid size of about 200 km and that we need to be very careful in choosing the grid size when applying this rheology to the numerical models of the SIZ.

4.1.1.2. Beaufort Sea

Unlike our result for the Sea of Okhotsk, Stern et al. (1995) used SAR-derived ice drift pattern at a grid spacing of 5 km in the Beaufort Sea to show that the area-averaged strain rate on about 100 km scale can parameterize opening (α_o) and closing (α_r) acceptably in terms of the deformation based on Hibler’s rheology. To investigate what caused the difference, we undertook similar analysis for the Beaufort Sea using AMSR-derived ice drift patterns for the same period as the Sea of Okhotsk analysis (January–March 2010). Five targeted areas were selected to cover a wide range of the Beaufort Sea. Each area is 5×5 grid cells, corresponding to $188 \times 188 \text{ km}^2$, and the locations are shown in Figure 1.

For the individual areas, we calculated $|\dot{\epsilon}|$ in two ways: from the area-averaged spatial derivatives of ice velocity ($\frac{\partial u_i}{\partial x_j}$) and from the area-averaged divergence ($\dot{\epsilon}_I$) and shear ($\dot{\epsilon}_{II}$). Closing and opening amount is calculated in the same way we did for the Sea of Okhotsk. The results of the former and latter methods are shown in Figures 11 and 12, respectively. Only data with strain rate $|\dot{\epsilon}| \geq 0.1 d^{-1}$ (as in Figure 8) are plotted

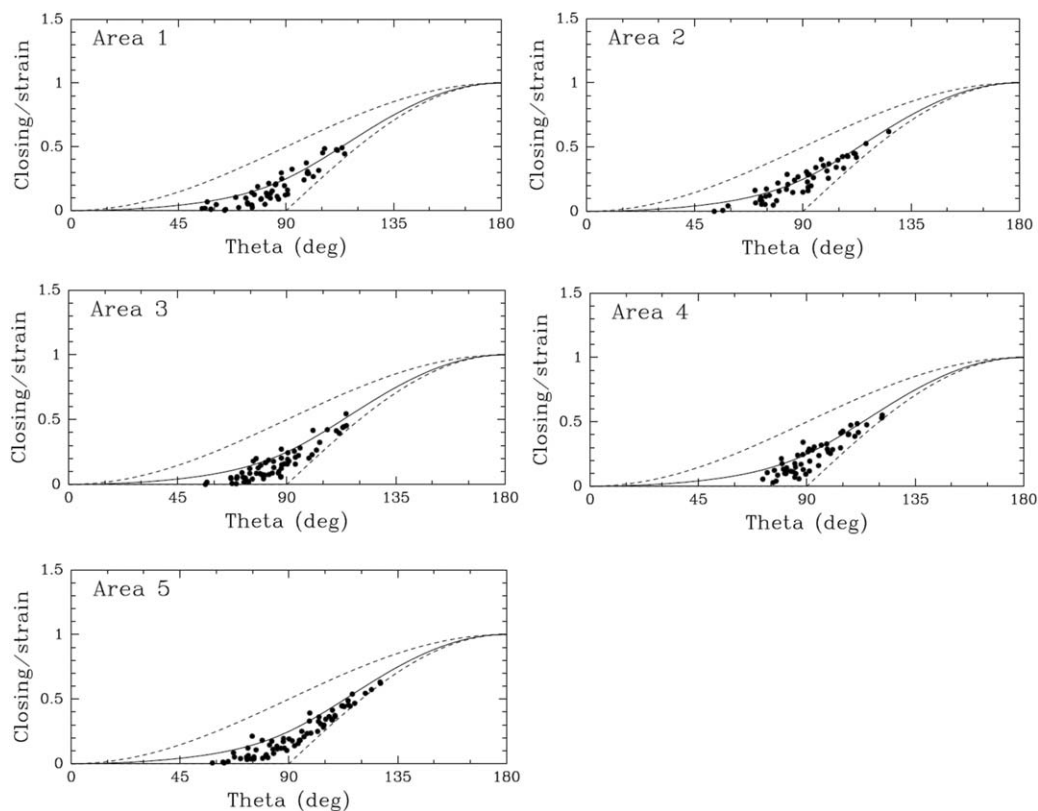


Figure 12. Same as Figure 10 except for the Beaufort Sea. The size of each area is all $188 \times 188 \text{ km}^2$.

to reduce the error due to the measurement accuracy. Therefore, the number of data points is somewhat less in Figure 11 than in Figure 12. It is impressive that the results for both methods are quite similar, unlike the Sea of Okhotsk, although the optimal e in Figure 12 tends to take somewhat higher values than 2 (Table 1). To clarify this outcome, the distribution of the strain ellipses within Area 1 on 26 January 2010, when the ice drift in the Beaufort Sea showed a systematic pattern on a large scale with high velocities ($\geq \sim 0.5 \text{ m s}^{-1}$), is depicted with the ice drift pattern in Figure 13 as an example.

Comparison between Figures 9 and 13 clearly shows that the horizontal variation in both the orientation and distortion of the strain ellipses is significantly less in the Beaufort Sea than in the Sea of Okhotsk. The coherency of the deformation field in the Beaufort Sea is found statistically from the good correlation between the time series of shear ($\dot{\epsilon}_{II}$) at the individual grid cells in Area 1. As many as 21 grid cells among 5×5 in Area 1 showed significantly good correlations at the 99% significance level. This is a contrast to the Sea of Okhotsk, where basically there appeared a significant correlation only between the neighboring grid cells. The situation was similar for the other areas and dates during the analysis period. This feature can be seen from the result that $|\dot{\epsilon}|$ did not change as much in the Beaufort Sea as in the Sea of Okhotsk (Table 1). This indicates that the subgrid-scale deformation field in the Beaufort Sea can be parameterized with mean ice drift, in a numerical sea ice model based on Hibler's rheology with a grid size of about 200 km, which is consistent with the results of Stern et al. (1995). The difference in strain rate variance between Figures 9 and 13 may explain why Hibler's rheology works better for the Beaufort Sea and not the Sea of Okhotsk.

4.1.2. Small Scale

Next, we show the results obtained from the ice drift derived from the coastal radar in the southernmost Sea of Okhotsk. The analytical method is basically the same as for the AMSR-derived ice drift. In our analysis, we consider one representative larger area of 20×20 grid cells and four representative smaller areas of 10×10 grid cells, corresponding to $26 \times 26 \text{ km}^2$ and $13 \times 13 \text{ km}^2$, respectively, to examine the scale dependence. Their locations are shown in Figure 14. α_r plots were made separately for these five areas on each day (9 days in total), using every 10 minutes data. As an example, the results on 12 February 2003 are shown in Figure 15. After calculating α_r in the two ways described in the previous section, we found that the use of area-averaged

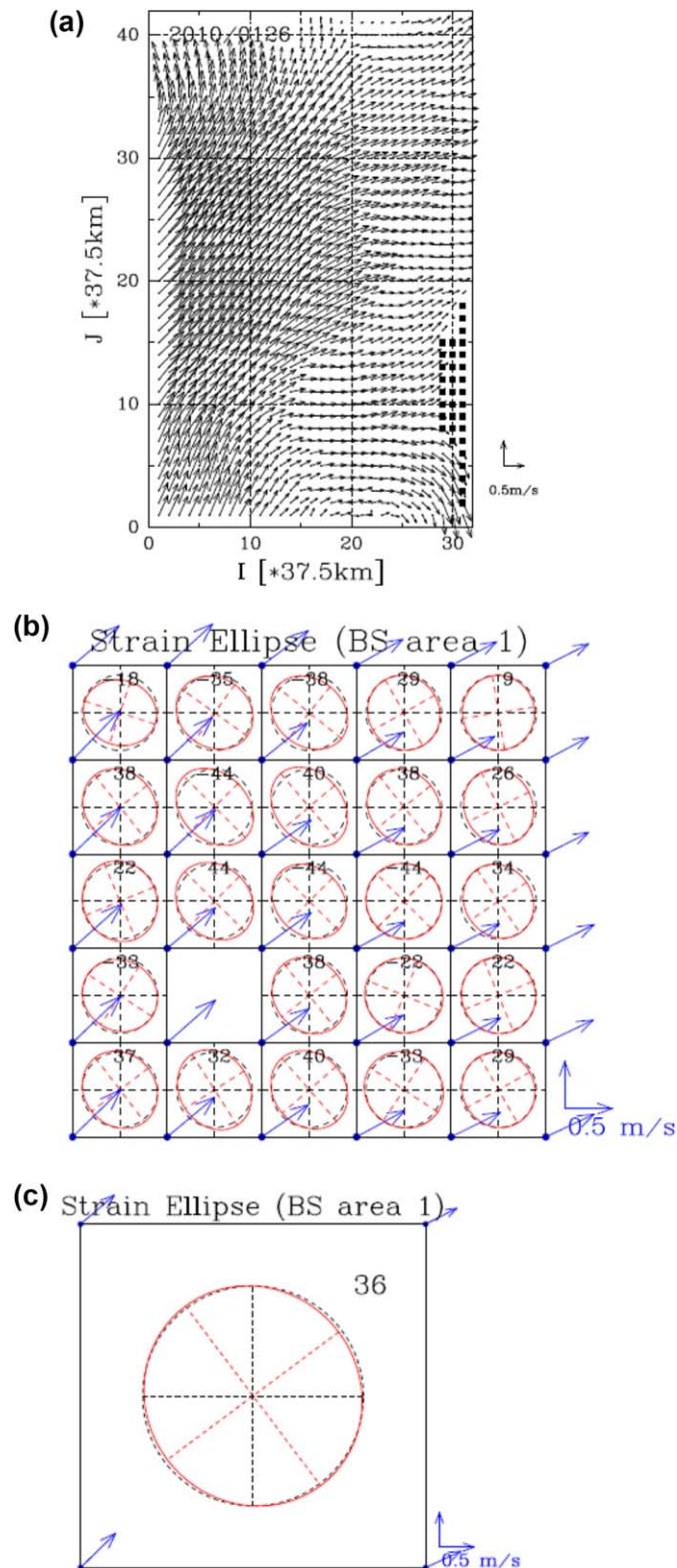


Figure 13. Characteristics of deformation field in the Beaufort Sea on 26 January 2010. The area is shown in Figure 1. Ice concentration was nearly 100%. (a) Ice drift pattern. The little black boxes to the right side denote land masks, corresponding to the northern coast of Alaska (Figure 1). Strain ellipse within Area 1 with ice velocity (blue arrows) and the value of φ , the orientation of the principal strain axes (degrees), shown for all grid cells (b) and (c) the area mean. Note the reduced variation in strain compared to Figure 9, and the similarity between area mean and individual ellipses at each grid cell.

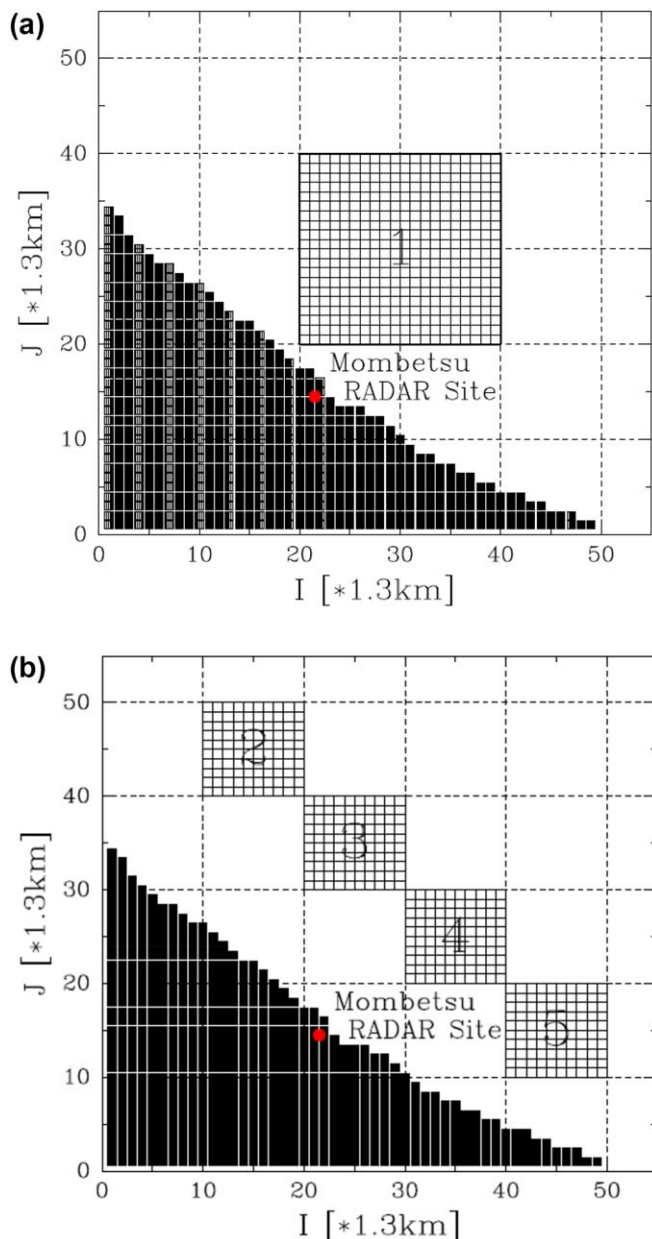


Figure 14. Five targeted areas used for the analysis of coastal radar data. See Figure 1 for the geographical location. (a) One larger square area with a side length of 26 km, containing 20×20 grid cells. (b) Four smaller square areas with a side length of 13 km, containing 10×10 grid cells.

increases. Considering that $|\dot{\epsilon}|$ is controlled mainly by the shear strain rate $\dot{\epsilon}_{II}$ in this region, this result seems reasonable.

4.2. Evaluation of Ice Strength Formulation

The area targeted for evaluating ice strength P was limited to Area 1 in the Sea of Okhotsk (Figure 7b) because this was the only region for which full data sets could be obtained. Figure 16 shows the temporal evolution of mean ice thickness (H_i) within Area 1 over the analysis period. Overall there is a long-term trend of increasing H_i from January to March. While this trend is reflected in thermodynamic growth, as described in section 2.3.2, the abrupt changes in H_i shown by arrows in the figure are considered to have occurred by ridging. Since ice thickness data were obtained sporadically, we took the averages of ice concentration and the closing amount for the time interval of the thickness data to calculate $|\dot{\epsilon}|_{\alpha_r, P}$ in equation

($23 \times 23 \text{ km}^2$ or $13 \times 13 \text{ km}^2$) velocities resulted in a significant underestimation of $|\dot{\epsilon}|$ in each case due to the large horizontal variation of the deformation field, presumably affected by diurnal tidal currents and large-scale wind patterns (Inoue, 2004). Therefore, the result by this method is shown only for Area 1 in Figure 15c, and the remaining figures in Figure 15 are all from the results obtained using the area-averaged $\langle \dot{\epsilon}_I \rangle$ and $\langle \dot{\epsilon}_{II} \rangle$.

It is impressive in Figure 15 that almost all points, except those for Figure 15c, lie approximately on the theoretical line of $e=2$. The fact that most of the plots are distributed around $\theta=90$ deg indicates that the shear component dominates in this region influenced by the strong coastal current. The optimal values of e were estimated to be 1.78 ± 0.19 for Area 1 and 1.73 ± 0.23 for Area 2–5 from a total of nine days. Considering that the mean magnitude of the strain rate is also similar ($2.56 \pm 1.12 \text{ d}^{-1}$ for Area 1 and $2.76 \pm 1.35 \text{ d}^{-1}$ for Area 2–5), there seems to be no significant difference in deformation properties between the 13 km and 26 km scales. Note that the optimal e is close to the $\sqrt{3}$ value predicted by the Von Mises criterion, justifying the treatment of sea ice area as a plastic material even on scales of a few tens of km in this region. Besides, since this is also close to 2, the validity of Hibler's formulation of the yield curve is to some extent confirmed on this horizontal scale.

However, although the result is consistent with the plastic behavior, again on this scale a numerical model would have difficulty in parameterizing the sub-grid scale (about 1 km) deformation field and then ridging due to the significant variation of the deformation field. α_r calculated from the grid scale (26 and 13 km) spatial derivatives of ice velocities deviated significantly from the theoretically predicted values, which are bounded by $e = 1$ to ∞ . This significant deviation is attributed to the underestimation of $|\dot{\epsilon}|$ by one fourth on average for 9 days, compared with that calculated from the sub-grid scale (1.3 km) ice velocities. Whereas $|\dot{\epsilon}|$ based on the sub-grid scale (1.3 km) ice velocities was $2.56 \pm 1.12 \text{ d}^{-1}$, that based on the grid scale (26 km) mean ice velocities was reduced to $0.66 \pm 0.29 \text{ d}^{-1}$ due to the large variation of the deformation field. This indicates that we need to be very careful in choosing the grid size when applying this rheology to the numerical models of the SIZ.

Another interesting result is that the optimal e values are highly correlated with mean $|\dot{\epsilon}|$ values, the correlation coefficients being 0.95 for Area 1 and 0.85 for Area 2–5. Since theoretically α_r must decrease as e increases with fixed θ , this means that the ratio of the convergence rate to the shear rate decreases as mean $|\dot{\epsilon}|$

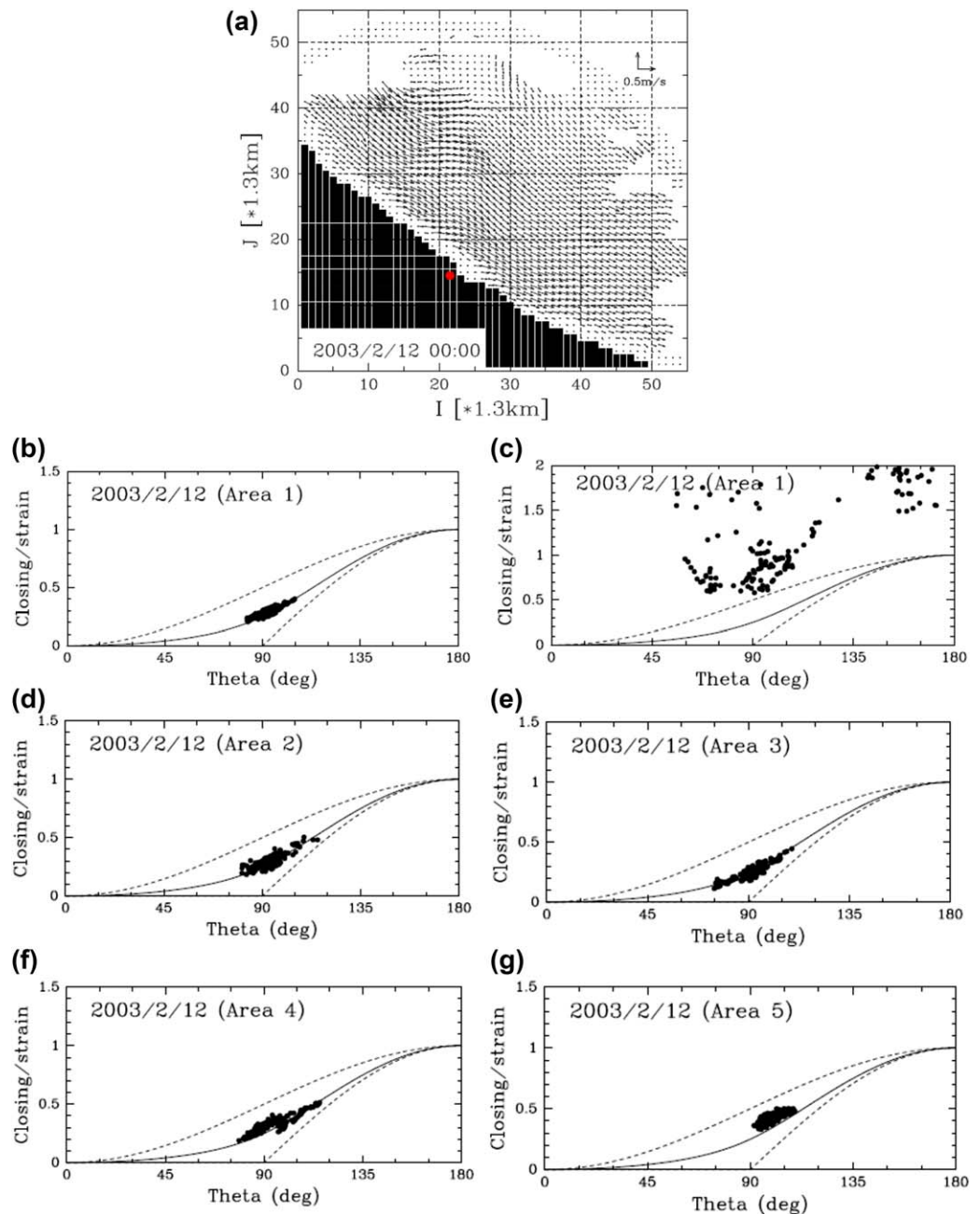


Figure 15. Characteristics of the deformation field near the coastal region of the southern Sea of Okhotsk on 12 February 2003. Each figure contains 144 points since ice drift pattern was obtained every 10 minutes. (a) Ice drift pattern at 00:00JST. Note the highly variable ice velocity distribution with substantial shear. (b) Closing amount/ $|\dot{\epsilon}|$, expressed by α_r , plotted as a function of θ every 10 minutes for Area 1 in Figure 14a. The plots are limited to the data with $|\dot{\epsilon}| \geq 0.1 \text{ d}^{-1}$. Note that $|\dot{\epsilon}|$ was calculated from the area-averaged $\langle \dot{\epsilon}_I \rangle$ and $\langle \dot{\epsilon}_{II} \rangle$. Theoretical lines of α_r for elliptical yield curves with aspect ratios of 1 (upper broken line), 2 (solid line), and ∞ (lower broken line) are also drawn. (c) Same as Figure 15b except that $|\dot{\epsilon}|$ was calculated with the area-averaged spatial derivatives $\langle \partial u_i / \partial x_j \rangle$. Note significant deviation from any theoretical lines because of the underestimation of $|\dot{\epsilon}|$. (d) Same as Figure 15b except for Area 2 in Figure 14b. (e) Same as Figure 15b except for Area 3 in Figure 14b. (f) Same as Figure 15b except for Area 4 in Figure 14b. (g) Same as Figure 15b except for Area 5 in Figure 14b.

(3), which is assumed to be the energy sink due to ridging. The value of h (mean ice thickness including open water) in equation (1) was given by $H_i \times A$. The scatter plots between the change in H_i (ΔH_i), given by the change in successive H_i , and the energy sink ($|\dot{\epsilon}| \alpha_r P$) are shown in Figure 17a. If the energy sink is well represented by equations (1) and (3), ΔH_i is expected to correlate with the energy sink estimated by $|\dot{\epsilon}| \alpha_r P$.

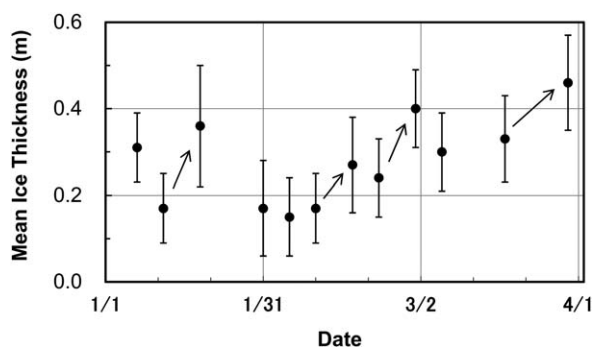


Figure 16. Temporal evolution of mean ice thickness averaged within Area 1 in Figure 7b. Error bars show a standard deviation within this area. Arrows point to an abrupt increase in mean ice thickness, probably caused by ridging processes.

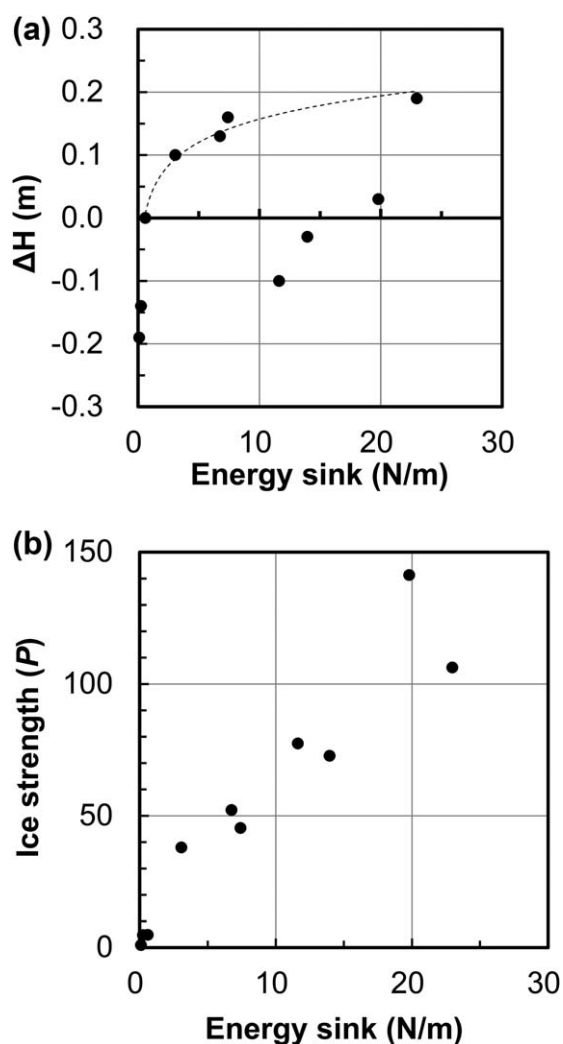


Figure 17. Evaluation of the ice strength P . (a) Changes in mean ice thickness (ΔH_i) as a function of the energy sink averaged for the time interval period ($\alpha_r |\dot{\epsilon}| P$). The broken line is a logarithmic fit to the largest energy sink events, expressed by $\Delta H_i = 0.0534 \ln(x) + 0.0342$, where x is the energy sink. (b) P calculated as a function of the energy sink.

Figure 17a shows that the calculated energy sink reflects ΔH_i well, especially for relatively large $\Delta H_i (\geq 0.1\text{m})$, although deviations are found at a few points. A logarithmic curve is drawn to fit the data using these large ΔH_i points and the point close to the origin. Since the potential energy used for ridging is proportional to the square of the ice thickness and the mean ice thickness H_i (estimated by equation (2)) tends to underestimate the ridged ice thickness, the nonlinear shape of the fitting function seems reasonable. Significant deviations from the fitted curve occurred on 22 February, 6 and 18 March, when ΔH_i corresponding to a large energy sink was not observed. On these days, although the original PALSAR images clearly show an increase in the ridged area from the previous images within Area 1, this property was not reflected directly on the area-averaged ΔH_i because of its large spatial variation. Therefore, we consider that Figure 17a generally supports the formulation and concept of equation (3), although great care is required to parameterize ridging in the model. P and the closing amount $\alpha_r |\dot{\epsilon}|$ almost equally contribute to the energy sink term in equation (3), with the correlation coefficient being a bit higher for P (0.95, see Figure 17b) than for $\alpha_r |\dot{\epsilon}|$ (0.80). Thus, it was found that the Hibler (1979) formulation of P seems reasonable in that the increase of ΔH_i is driven by the energy sink to which P contributes significantly ($p < 0.01$), as far as the representation of the ice strength related to ridging is concerned. However, it should be noted that P^* , which essentially determines the magnitude of the ice strength, was not verified here and needs to be investigated by other methods.

5. Discussion

Here we discuss two important issues that have arisen from our study: the difference between the Sea of Okhotsk and the Beaufort Sea, and the applicability to the rheology parameterized for longer time scales. Regarding the former issue, factors responsible for the different horizontal variability of the deformation field between these two regions could be related to the ice conditions including floe size distribution and compactness. MODIS images show that whereas vast (≥ 1 km) and compacted ice floes, accompanied with long linear cracks, are dominant in the Beaufort Sea, relatively small (≤ 1 km) and less compacted ice floes are usually found in the Sea of Okhotsk (Figure 4b; Toyota et al., 2007). It is likely that such different ice conditions impact the dynamical properties of sea ice between the two regions. The fact that the formulation of the yield curve holds true for scales of 13, 26, and 200 km in the Sea of Okhotsk suggests that dynamical properties might be scale invariant within the range of these scales. Considering that floe size distribution in this region has a self-similarity for floes larger than about 40 m (Toyota et al., 2006), this result seems reasonable. The plastic rheology of sea ice is based on the idea that the aggregate of granular media (floes) behaves like a plastic material (Coon, 1974; Feltham, 2008) and therefore floe size distribution must be an important factor that determines the rheology. On the other hand, in the Beaufort Sea where linear cracks are common on scales larger than the floe size, it might be possible that the energy sinks due to sliding motion cannot be neglected and thereby the teardrop or lens-shaped curve might be more appropriate than an ellipse, as discussed by Ukita and Moritz (1995). Overall it is found that the observed α_r in Figures 11 and 12 tends to take somewhat

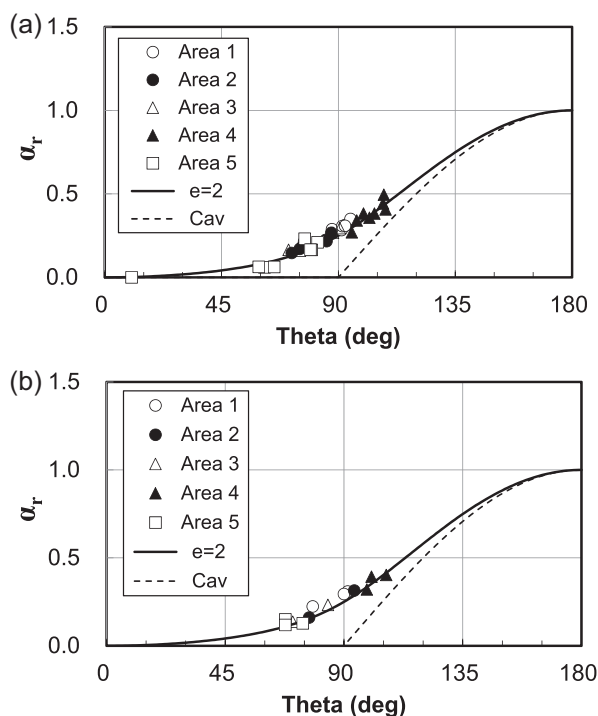


Figure 18. Closing amount/ $|\dot{\epsilon}|$, expressed by α_r , as a function of θ for the five areas in Figure 7b in the Sea of Okhotsk for (a) 10 day mean data and (b) monthly mean data. Theoretical lines for an ellipse with an aspect ratio of 2 (thick solid line) and ∞ (broken line) are also drawn. The curve with an aspect ratio of ∞ corresponds to cavitating fluid proposed by Flato and Hibler (1992). The number of data points is 35 for 10 day mean and 13 for monthly mean.

lower values (i.e., higher values of e) than the theoretical line for an ellipse with $e=2$. Such behavior is unique to the teardrop or lens shaped yield curve (Rothrock, 1975). This is especially true for $\theta < 90$ deg. This seems consistent because the energy sink due to ridging would decrease if part of the total kinetic energy is transformed into sliding friction between floes. The fact that optimal e takes a higher value at Area 3 (2.9) and 5 (3.0), closer to the coast, than at Area 2 (2.2) and 4 (2.5) (Table 1) supports this idea because this effect is expected to be larger near the coast.

Next, we examine the validity of this rheology for the longer time scales necessary in climate studies. So far, we have shown the results from daily calculations. To make the numerical sea ice model more simplistic and efficient for long-term climate studies, Flato and Hibler (1992) proposed the concept of ‘cavitating’ fluid behavior whereby the ice pack resists neither divergence nor shear, but importantly resists convergence. This idea corresponds to an elliptic yield curve with $e=\infty$, i.e., $\alpha_r(\theta)=0$ for $\theta < 90$ deg and $\alpha_r(\theta)=-\cos\theta$ for $90 \leq \theta \leq 180$ deg. To check if this model is reasonable, we calculated 10 day mean and monthly mean deformation components by taking the temporal averages of the area-averaged divergence $\langle \dot{\epsilon}_I \rangle$ and shear $\langle \dot{\epsilon}_{II} \rangle$ components and the closing amount to obtain α_r across the five areas in the Sea of Okhotsk. θ was determined using the temporal average $\langle \dot{\epsilon}_I \rangle$ and $\langle \dot{\epsilon}_{II} \rangle$. α_r was obtained for all areas and plotted together as a function of θ in Figure 18a as the 10 day mean and in Figure 18b as the monthly mean. Both figures clearly show that almost all data lie on the theoretical curve of the ellipse with $e=2$, far from the curve for a cavitating fluid ($e=\infty$). The curve fit appears to be even better than the daily data (Figure 10), possibly resulting from an offset error during averaging. This indicates that Hibler’s formulation

of rheology is at least applicable on monthly time scales and the shape of the yield curve shows no change for time scale. Sea ice area should be treated as a plastic material, not a cavitating fluid: i.e., the contribution of the large-scale shear component to ridging should not be neglected especially in higher resolution models.

6. Conclusions

The validity of the formulation of the sea ice rheology proposed by Hibler (1979) was investigated on the scale of a few hundreds of kilometers for the Sea of Okhotsk, a region that is characterized in winter as a typical SIZ. The analysis was based on sea ice velocity, concentration and thickness distribution data derived from satellite data. To examine if there is scale dependence in the applicability of the rheology, additional ice drift data sets derived from a coastal radar operated at the southernmost Sea of Okhotsk, covering about 70 km area from the coast, were also analyzed. Our evaluation focused on the nature of the yield curve, i.e., its shape and the ice strength P , which determines the magnitude of the yield curve. Following Rothrock (1975), we assumed that the total work rate per unit area done by the deformation field be equated to the energy sink due to ridging. To determine the shape of the yield curve, we used the theory proposed by Rothrock (1975) and the method applied to the Beaufort Sea by Stern et al. (1995), which can provide guidance about the effectiveness of parameterizing sub-grid scale deformation in numerical sea ice models. Since plasticity theory states that in general the yield curve should be expressed by the ellipse, with an aspect ratio e of 1.7–2.0, we attempted to show how close to this value the optimal e is for the assumption of an elliptic curve, following the Stern et al. (1995) methodology. To compare with the results of Stern et al. (1995), we extended our analysis to the Beaufort Sea for the same analysis period as our Sea of Okhotsk study.

To understand if the Hibler (1979) formulation of ice strength P is appropriate, we show how well correlated the energy sink, expressed by $|\dot{\epsilon}| \alpha_r P$ (equation (3)), where P was calculated with the area-averaged A and H_i ,

is with the area-averaged ΔH_i which is considered to represent the degree of ridging. For this purpose, we also evaluated the retrieval of ice thickness from PALSAR data against a 1-D thermodynamic model driven by ERA-Interim data sets (equation (2)), obtaining good agreement for level ice thickness, and found the model supports the interpretation that the PALSAR retrieval is providing level ice thickness.

Our results found an optimal e to be in the range 1.7–2.0 over a 150–200 km scale, 1.78 ± 0.19 on a 26 km scale, and 1.73 ± 0.23 on a 13 km scale for the Sea of Okhotsk. There was no time dependence for this result. Since these values are close to the plasticity theory of Tresca and Von Mises, this result justifies the treatment of sea ice as a plastic material in this region, and supports Hibler's formulation of the yield curve (an ellipse with $e = 2$) over a wider range of scales. The result for the 150–200 km scale is consistent with the result of Stern et al. (1995). However, significant difference between the Sea of Okhotsk and the Beaufort Sea arose when we calculated $|\dot{\epsilon}|$ using the area-averaged spatial derivatives of ice velocity $\langle \partial u_i / \partial x_j \rangle$, instead of the area-averaged divergence $\langle \dot{\epsilon}_i \rangle$ and shear $\langle \dot{\epsilon}_{II} \rangle$. Whereas the result did not essentially change in the Beaufort Sea, underestimation of $\langle \dot{\epsilon} \rangle$ in the Sea of Okhotsk induced significant deviation from theory, resulting from the large variation in its deformation field. We infer that the ice conditions such as compactness, floe size distribution, and ocean currents are the most likely factors responsible for such a difference. This means that careful treatment is required to reproduce the sub-grid scale deformation in numerical modelling of the SIZ. It is interesting to note that optimal e for the Sea of Okhotsk was closer to the value of 2 used by Hibler (1979), relative to the values for the Beaufort Sea, which suggests that the yield process may be different between these two regions. This likely reflects the different ice conditions in the two regions.

We obtained a similarly supportive result for the formulation of P , in that the energy sink calculated as a function of P is reasonably correlated with mean ice thickness change, ΔH_i , especially for relatively large values of ΔH_i . However, there were some cases where ΔH_i did not respond to the relatively large energy sinks suggested by the observed strain-rate. We infer that this was mainly caused by localized ridging processes that cannot be represented from large-scale deformation. Therefore, this result also cautions us about taking careful treatment when parameterizing the sub-grid scale ridging in numerical models. Determining P^* in the formulation of P is a separate issue, considered in other papers, and P^* needs to be tuned properly to predict the ridging processes.

To summarize, the results obtained on both larger (~ 150 – 200 km) and smaller (~ 20 km) scales provided supportive evidence for the treatment of sea ice area as a plastic material and Hibler's formulation of ice rheology in the Sea of Okhotsk. However, the results also highlight the difficulty in parameterizing local scale ridging processes in the numerical models, due to the large variation of the deformation field. Considering the variability of ice drift pattern and floe-size distribution common to SIZs, our results are expected to apply to other SIZs. While clearly important to examine the sea ice rheology for the SIZ at the geophysical scale, previous attempts have been limited both temporally and regionally so far. Therefore, further investigation is needed to fully develop its parameterization into numerical sea ice models of the SIZ.

Acknowledgments

This work was supported by JSPS KAKENHI 18510003, 21510002, 2451000102, and 16K00511 [Grant-in-Aid for Scientific Research (C)]. ALOS/PALSAR images were provided by JAXA through the ALOS Research Project (PI No.573). The International Space Science Institute (Bern, Switzerland) is also acknowledged for supporting this study via project #137. Observation in the Sea of Okhotsk was conducted in collaboration with P.V. "Soya." Critical reading of the manuscript and beneficial comments by Jennifer Hutchings and proofreading by Guy Williams were very helpful to improve the paper. Discussions with Humio Mitsudera and Yoshimasa Matsumura, and valuable comments by two reviewers are also acknowledged. Eriko Ishikawa helped us draw some figures. We express our sincere gratitude to them. Data Base of AMSR-E brightness temperature: https://nsidc.org/data/AE_S16

References

- Agnew, T., Le, H., & Hirose, T. (1997). Estimation of large scale sea-ice motion from SSM/I 85.5 GHz imagery. *Annals of Glaciology*, 25, 305–311.
- Cavalieri, D. J., & Parkinson, C. L. (2012). Arctic sea ice variability and trends, 1979–2010. *The Cryosphere*, 6, 881–889.
- Collins, M. J., & Emery, W. J. (1988). A computational method for estimating sea ice motion in sequential Seasat synthetic aperture radar imagery by matched filtering. *Journal of Geophysical Research*, 93(C8), 9241–9251.
- Coon, M. D. (1974). Mechanical behavior of compacted Arctic ice floes. *JPT Journal of Petroleum Technology*, 26, 466–470.
- Coon, M. D., Maykut, G. A., Pritchard, R. S., Rothrock, D. A., & Thorndike, A. S. (1974). Modeling the pack-ice as an elastic-plastic material. *AID-JEX Bulletin*, 24, 1–105.
- Dansereau, V., Weiss Saramito, J. P., Lattes, P., & Coche, E. (2017). Icebridges and ridges in the Maxwell-EB sea ice rheology. *The Cryosphere*, 11, 2033–2058. <https://doi.org/10.5194/tc-11-2033-2017>
- Emery, W. J., Fowler, C. W., Hawkins, J., & Preller, R. H. (1991). Fram Strait satellite image-derived ice motions. *Journal of Geophysical Research*, 96(C3), 4751–4768.
- Feltham, D. L. (2008). Sea ice rheology. *Annual Review of Fluid Mechanics*, 40, 91–112.
- Fily, M., & Rothrock, D. A. (1987). Sea ice tracking by nested correlations. *IEEE Transactions on Geoscience and Remote Sensing*, GE-25, 570–580.
- Fily, M., & Rothrock, D. A. (1990). Opening and closing of sea ice leads: Digital measurements from Synthetic Aperture Radar. *Journal of Geophysical Research*, 95(C1), 789–796.
- Flato, G. M., & Hibler, W. D., III. (1992). Modeling pack ice as a cavitating fluid. *Journal of Physical Oceanography*, 22, 626–651.
- Geiger, C. A., Hibler, W. D., III, & Ackley, S. F. (1998). Large-scale sea ice drift and deformation: Comparison between models and observations in the western Weddell Sea during 1992. *Journal of Geophysical Research*, 103(C10), 21893–21913.

- Hibler, W. D., III. (1977). A viscous sea ice law as a stochastic average of plasticity. *Journal of Geophysical Research*, 82(27), 3932–3938.
- Hibler, W. D., III. (1979). A dynamic thermodynamic sea ice model. *Journal of Physical Oceanography*, 9, 815–846.
- Hibler, W. D., III. (2001). Modeling the formation and evolution of oriented fractures in sea ice. *Annals of Glaciology*, 33, 157–164.
- Hibler, W. D., III, & Schulson, E. M. (1997). On modeling sea-ice fracture and flow in numerical investigations of climate. *Annals of Glaciology*, 25, 26–32.
- Hibler, W. D., III, & Schulson, E. M. (2000). On modeling the anisotropic failure and flow of flawed sea ice. *Journal of Geophysical Research*, 105(C7), 17105–17120.
- Hibler, W. D., III, & Vavrus, S. J. (2012). Pre-industrial multiple equilibrium sea-ice flow states due to plastic ice mechanics. *Cold Regions Science and Technology*, 76–77, 92–108.
- Hunke, E. C., & Dukowicz, J. K. (1997). An elastic-viscous-plastic model for sea ice dynamics. *Journal of Physical Oceanography*, 27, 1849–1867.
- Hunke, E. C., Lipcome, W. H., & Turner, A. K. (2010). Sea-ice models for climate study: Retrospective and new directions. *Annals of Glaciology*, 56(200), 1162–1172.
- Hutchings, J. K., Heil, P., & Hibler, W. D., III. (2005). Modelling linear kinematic features in sea ice. *Monthly Weather Review*, 133, 3481–3497.
- Inoue, J. (2004). Effects of tidal current and wind on the coastal sea-ice motion in the Sea of Okhotsk [in Japanese with English summary]. *Umi to Sora*, 79(2–3), 57–64.
- Ip, C. F., Hibler, W. D., III, & Flato, G. M. (1991). On the effect of rheology on seasonal sea-ice simulations. *Annals of Glaciology*, 15, 17–25.
- Ishikawa, M., Takatsuka, T., Daibo, T., & Shirasawa, K. (2004). *Distribution of pack ice in the Okhotsk Sea off Hokkaido observed using a sea-ice radar network, January–April 2003* (Low Temperature Science, Ser. A., Data Rep. 62, pp. 19–48). Sapporo City, Japan: Institute of Low Temperature Science, Hokkaido University.
- Kachanov, L. M. (1971). *Foundations of the theory of plasticity*. (478 pp.). Amsterdam, the Netherlands: North-Holland Publishing Company.
- Kim, Y.-S. (1992). *Estimate of heat transport across the sea surface near Japan with bulk methods* (D. Sci., 124 pp.). Tokyo, Japan: Univ. of Tokyo.
- Kimura, N., Nishimura, A., Tanaka, Y., & Yamaguchi, H. (2013). Influence of winter sea ice motion on summer ice cover in the Arctic. *Polar Research*, 32, 20193. <http://doi.org/10.3402/polar.v32i0.20193>
- Kimura, N., & Wakatsuchi, M. (2000). Relationship between sea-ice motion and geostrophic wind in the Northern Hemisphere. *Geophysical Research Letters*, 27(22), 3735–3738.
- Kreyscher, M., Harder, M., Lemke, P., & Flato, G. M. (2000). Results of the sea ice model intercomparison project: Evaluation of sea ice rheology schemes for use in climate simulations. *Journal of Geophysical Research*, 105(C5), 11299–11320.
- Kwok, R., Schweiger, A., Rothrock, D. A., Pang, S., & Kottmeier, C. (1998). Sea ice motion from satellite passive microwave imagery assessed with ERS SAR and buoy motions. *Journal of Geophysical Research*, 103(C4), 8191–8214.
- Leppäranta, M. (2005). *The drift of sea ice* (266 pp.). Chichester, UK: Springer-Praxis Publishing Ltd.
- Losch, M. D., Menemenlis, J.-M., Campin, P., Heimbach, C., & Hill, (2010). On the formation of sea-ice models. Part I: Effects of different solver implementations and parameterizations. *Ocean Modelling*, 33, 129–144.
- Massom, R. (2006). Basic remote-sensing principles relating to the measurement of sea ice and its snow cover. In D. Lubin & R. Massom (Eds.). *Polar remote sensing Vol. I: Atmosphere and oceans* (pp. 356–380). Chichester, UK: Praxis Publishing Ltd.
- Maykut, G. A. (1982). Large-scale heat exchange and ice production in the central Arctic. *Journal of Geophysical Research*, 87(C10), 7971–7984.
- Maykut, G. A., & Church, P. E. (1973). Radiation climate of Barrow, Alaska, 1962–66. *Journal of Applied Meteorology*, 12(4), 620–628.
- Miller, P. A., Laxon, S. W., & Feltham, D. L. (2005). Improving the spatial distribution of modeled Arctic sea ice thickness. *Geophysical Research Letters*, 32, L18503. <https://doi.org/10.1029/2005GL023622>
- Moritz, R. E., & Ukita, J. (2000). Geometry and the deformation of pack ice: I. A simple kinematic model. *Annals of Glaciology*, 31, 313–322.
- Ninnis, R. M., Emery, W. J., & Collins, M. J. (1986). Automated extraction of pack ice motion from advanced very high resolution radiometer imagery. *Journal of Geophysical Research*, 91(C9), 10725–10734.
- Ohshima, K. I., Nishashi, S., Hashiya, E., & Watanabe, T. (2006). Interannual variability of sea ice area in the Sea of Okhotsk: Importance of surface heat flux in fall. *Journal of Meteorological Society of Japan*, 84(5), 907–919.
- Rothrock, D. A. (1975). The energetics of the plastic deformation of pack ice by ridging. *Journal of Geophysical Research*, 80(33), 4514–4519.
- Spren, G., Kaleschke, L., & Heygster, G. (2008). Sea ice remote sensing using AMSR-E 89-GHz channels. *Journal of Geophysical Research*, 113, C02503. <https://doi.org/10.1029/2005JC003384>
- Stern, H. K., Rothrock, D. A., & Kwok, R. (1995). Open water production in Arctic sea ice: Satellite measurements and model parameterizations. *Journal of Geophysical Research*, 100(C10), 20601–20612.
- Stroeve, J. C., Serreze, M. C., Holland, M. M., Key, J. E., Malanik, J., & Barrett, A. P. (2012). The Arctic's rapidly shrinking sea ice cover: A research synthesis. *Climatic Change*, 110, 1005–1027. <https://doi.org/10.1007/s10584-011-0101-1>
- Sumata, H., Gerdes, R., Kauker, F., & Karcher, M. (2015). Empirical error functions for monthly mean Arctic sea-ice drift. *Journal of Geophysical Research: Oceans*, 120, 7450–7475. <https://doi.org/10.1002/2015JC011151>
- Tabata, T. (1975). Sea-ice reconnaissance by radar. *Journal of Glaciology*, 15(73), 215–224.
- Thorndike, A. S. (1986). Kinematics of sea ice. In N. Untersteiner (Ed.), *The geophysics of sea ice*, (NATO ASI, Ser. B, Vol.146, chap.7, pp.489–549). New York: Plenum.
- Thorndike, A. S., Rothrock, D. A., Maykut, G. A., & Colony, R. (1975). The thickness distribution of sea ice. *Journal of Geophysical Research*, 80(33), 4501–4513.
- Toyota, T., Kawamura, T., Ohshima, K. I., Shimoda, H., & Wakatsuchi, M. (2004). Thickness distribution, texture and stratigraphy, and a simple probabilistic model for dynamical thickening of sea ice in the southern Sea of Okhotsk. *Journal of Geophysical Research*, 109, C06001. <https://doi.org/10.1029/2003JC002090>
- Toyota, T., Kawamura, T., & Wakatsuchi, M. (2000). Heat budget in the ice cover of the southern Okhotsk Sea derived from in-situ observations. *Journal of Meteorological Society of Japan*, 78(5), 585–596.
- Toyota, T., Nakamura, K., Uto, S., Ohshima, K. I., & Ebuchi, N. (2009). Retrieval of sea ice thickness distribution in the seasonal ice zone from air-borne L-band SAR. *International Journal of Remote Sensing*, 30(12), 3171–3189.
- Toyota, T., Ono, S., Cho, K., & Ohshima, K. I. (2011). Retrieval of sea ice thickness distribution in the Sea of Okhotsk from ALOS/PALSAR backscatter data. *Annals of Glaciology*, 52(57), 177–184.
- Toyota, T., Takatsuchi, S., & Nakayama, M. (2006). Characteristics of sea ice floe size distribution in the seasonal ice zone. *Geophysical Research Letters*, 33, L02616. <https://doi.org/10.1029/2005GL024556>
- Toyota, T., Takatsuchi, S., Tateyama, K., Naoki, K., & Ohshima, K. I. (2007). Properties of sea ice and overlying snow in the southern Sea of Okhotsk. *Journal of Oceanography*, 63, 393–411.

- Toyota, T., & Wakatsuchi, M. (2001). Characteristics of the surface heat budget during the ice-growth season in the southern Sea of Okhotsk. *Annals of Glaciology*, *33*, 230–236.
- Ukita, J., & Moritz, R. E. (1995). Yield curves and flow rules of pack ice. *Journal of Geophysical Research*, *100*(C3), 4545–4557.
- Wang, K. (2007). Observing the yield curve of compacted pack ice. *Journal of Geophysical Research*, *112*, C05015. <https://doi.org/10.1029/2006JC003610>
- Wilchinsky, A. V., & Feltham, D. L. (2004). Dependence of sea ice yield-curve shape on ice thickness. *Journal of Physical Oceanography*, *34*, 2852–2856.
- Worby, A. P., Jeffries, M. O., Weeks, W. F., Morris, K., & Jana, R. (1996). The thickness distribution of sea ice and snow cover during late winter in the Bellingshausen and Amundsen Seas, Antarctica. *Journal of Geophysical Research*, *101*(C12), 28441–28455.
- Zhang, J., & Rothrock, D. A. (2005). Effect of sea ice rheology in numerical investigations of climate. *Journal of Geophysical Research*, *110*, C08014. <https://doi.org/10.1029/2004JC002599>